TIMING NOISE OF PSR B0329+54 AND ITS FREQUENT MODE CHANGING

A THESIS SUBMITTED TO THE UNIVERSITY OF MANCHESTER
FOR THE DEGREE OF MASTER OF PHILOSOPHY
IN THE FACULTY OF SCIENCE AND ENGINEERING

2018

By

Joseph A. Kwofie

School of Physics and Astronomy

Contents

Word Count: 28,562

List of Tables

List of Figures

The University of Manchester

ABSTRACT OF THESIS submitted by Joseph Amihere Kwofie for the degree of Master of Philosophy and entitled

"Timing Noise of PSR B0329+54 and its Frequent Mode Changing"

January 2018.

Pulsars are famed for their highly precise frequency of rotation and periodic pulses. The time of arrival of their periodic pulses can generally be predicted to a high precision, but not perfectly. Deviation of the times of arrival (TOA) of the pulses from prediction is common to many known pulsars. One type of the deviation known as timing noise is characterised by unexplained wandering of pulse phases relative to a simple model. It is believed that this timing noise holds clues to the physics of the stellar interior. Also, if the timing noise is properly modelled, the times of arrival can be improved to allow pulsars to be used as precise clocks. Observations of some pulsars have shown that the spin-down varies with time and it is also linked with perturbations of the conditions in the pulsar's magnetosphere. This link, in the case of PSR B0329+54, was investigated in this work. PSR B0329+54 is known to undergo mode changes, in which a sequence of pulses has one of the two stable shapes. Firstly, it was demonstrated that the systematic offset of the abnormal mode TOAs from normal mode TOAs is associated with magnetospheric mode changing, rather than the effect of template matching. Secondly, the shape of each pulse profile was quantified using the fractional occurrence of one of the stable pulse shapes and the variations of the spin-down rate was obtained by modelling the timing noise with Gaussian process regression. There was a strong correlation between the fractional occurrence and the timing noise during the section of periodic modulation for which a correlation coefficient of 0.6 was found. There was also a strong correlation

between the fractional occurrence and the spin-down variation during the periodic modulation. These results show that the rate of change between these pulse shapes is itself changing with time, and corresponds to variations in the spin-down rate.

Declaration

No portion of the work referred to in this thesis has been submitted in support of an application for another degree or qualification of this or any other university or other institute of learning.

Copyright

Acknowledgements

I would like to thank my supervisor Benjamin Stappers for his support, patience, guidance and understanding. He has inspired confidence in me which I will carry along for the rest my life.

I thank all members of the pulsar group, particularly Benetge Perera, Benjamin Shaw and Robert Lyon for helping me with the tools, techniques and theoretical framework that I needed to complete this work. I also cherish fond memories of social moments in the company of Thomas Scragg, Xiaojin Liu, Chia Min Tan and Charlie Walker. Those moment gave me great relief to carry on and I am very grateful.

Finally, I would like to express my sincere gratitude to the Newton Fund through the Development in Africa with Radio Astronomy (DARA) project for funding my masters study in the The University of Manchester.

Chapter 1

Introduction

1.1 Background

Since the discovery of the first pulsar through its radio pulses, which appeared with a remarkably precise period, the best explanation given for the origin of these pulses is that they are emitted by a rotating neutron star (Hewish et al., 1968; Gold, 1968). Neutron stars are incredibly dense, having a typical mass of $1.46\,M_{\odot}$ and a diameter of about 20 km (Lorimer & Kramer, 2005a). Currently, there are about 2600[1] known pulsars each rotating with highly stable spin periods ranging between approximately 1 ms and 10 s (Manchester et al., 2005). As a pulsar rotates, its beam of radio waves momentarily aligns with an observer's line of sight once every rotation, leading to the characteristic periodic pulses.

The existence of neutron stars had been proposed long before their discovery by Baade & Zwicky (1934) as the final transition of stars into very small compact objects. However, there was little hope of observing them due to their small size, despite having a surface

[1] See http://http://www.atnf.csiro.au/research/pulsar/psrcat for up-to-date catalog

temperature that is about hundred times greater than that of the Sun (see e.g. Tsuruta et al., 1972). Nevertheless, Pacini (1967) ascribed the source of energy in the Crab Nebula to a neutron star before any observational evidence was found. These proposals received their observational evidence from the discovery of the first pulsar and the subsequent discovery of the Crab pulsar (Hewish et al., 1968; Staelin & Reifenstein, 1968). Today, it is commonly believed that neutron stars are likely the final products of medium mass stars (8-20 $M_{\odot}$). The total collapse of a star due to the gravitational force is prevented by thermal and radiation pressure. This balance, known as hydrostatic equilibrium, is maintained until it ends its life in a violent explosion known as a supernova (details can be found in Imshennik, 1995, for example). The supernova event is survived by a compact core that conserves the high magnetic field and the angular momentum of the progenitor stars (Baade & Zwicky, 1934).

It is difficult to find a physical model that completely describes the observed characteristics of all pulsars. Unlike luminous stars, an isotropic source does not explain the periodic narrow pulses. Rather, a directional beam of radio waves has become an imperative option. Consistent with this, Radhakrishnan et al. (1969) showed from the observation of the Vela pulsar that the plane of polarisation rotated uniformly in polarisation angle during the pulse. Hence a realistic model that explains the periodic pulses from the rotating neutron stars, required a localised region within some 100 stellar radii (e.g. Gil et al., 1993; Kijak & Gil, 1997), and beaming in a direction inclined to the spin axis. Similar to a rotating magnet with its magnetic axis inclined relative to its rotation axis, pulsars emit radiation primarily at the expense of rotational kinetic energy (see Jackson, 1962).

Regardless of the spin period of pulsars, their mean flux density, S_{mean}, can be expressed as a power law function of the frequency, f, of observation (i.e. $S_{mean} \propto f^{\alpha}$)

with typical spectral index $\alpha = -1.8 \pm 0.2$ (Maron et al., 2000). Although pulsars are usually observed in the radio window between 100 MHz and 100 GHz (e.g. Kramer et al., 1997; Lorimer & Kramer, 2005a), some have been observed in the high energy region of the electromagnetic spectrum (e.g. Abdo et al., 2009). In addition to emission powered by the loss of rotational kinetic energy (§1.2) some pulsars exhibit other emission mechanisms due to their surface temperature and/or by accretion of matter from their companions (Grindlay et al., 2002; Pons et al., 2002). These emissions are often at X-ray energies.

The majority of pulsars are located in the Galactic plane, consistent with the distribution of main sequence stars (e.g. Keane et al., 2014). However, the expected radial distribution of stars about the Galactic centre is at odds with observation, which shows pulsars concentrated around our solar system. Although there is credible evidence of large number of neutron stars residing close to the Galactic centre, only 6 pulsars and 1 magnetar are known to be located within 36 pc from the Galactic centre (Chennamangalam & Lorimer, 2014; Keane et al., 2014). The small population of pulsars observed in the Galactic centre indicates the difficulty of finding them within this region, due to high scattering effects by the interstellar medium (Cordes & Lazio, 1997). Recently, Chennamangalam & Lorimer (2014) instead suggested an intrinsic deficiency of pulsars as a possible reason. The estimated 30,000 pulsars to be found by the more sensitive Square Kilometre Array (SKA) telescope, will provide better insight into the distribution of the pulsars (Keane et al., 2014).

In spite of their peculiar characteristics, significant similarities and differences provide a basis for classifying pulsars into groups; these are better illustrated on the period-period derivative diagram (Figure 1.1). There are two principal groups based on their spin periods: *normal* pulsars and the *millisecond* pulsars. The spin periods of the normal pulsars

are usually above 10 ms while those of the millisecond pulsars fall below 10 ms. The latter group of pulsars also have more stable spin period derivatives (10^{-21} - 10^{-17} ss^{-1}), lower magnetic field strength (of the order of 10^8 G) and are much older than the normal pulsars. Most millisecond pulsars are known to have binary companions. Another group of pulsars are rather marked by very strong magnetic fields, typically 10^{14} G and high spin period, typically between 6-12 s (Lyne & Graham-Smith, 2005), are classified as *magnetars* (top-right of Figure 1.1). Further classifications can be derived among normal pulsars based on the manner and the extent to which they exhibit quasi-discrete emission mode changes. For example, some pulsars are known to 'switch off' occasionally, a phenomenon known as nulling (Backer, 1970). A few pulsars, such as PSR B1931+24, that 'switch off' for a time scale between 25-35 days and resume emitting pulses for 5-10 days, are referred to as *intermittent pulsars* (Kramer et al., 2006).

A plausible evolutionary path can be traced from the region with greater concentration of supernova remnants, where pulsars are thought to be born. Pulsars spin down gradually as they lose angular momentum, until they are no longer detectable (lower right in Figure 1.1) (Lorimer & Kramer, 2005a). Millisecond pulsars are old neutron stars that are "recycled" through their binary companions (Alpar et al., 1982). This means that late in their normal pulsar lives, they may accrete matter from their evolved companion stars, gain angular momentum, and spin up to millisecond rotational periods with stable spin-down rates (i.e. lower left of Figure 1.1) (see Bhattacharya & van den Heuvel, 1991, for details of possible ways of forming millisecond pulsars with binaries). A key challenge to understanding their evolution is the low magnetic field. Loss of their magnetic field is attributed to either a natural decay over the time span 10^{10} years or to processes during the accretion phase (Bisnovatyi-Kogan & Komberg, 1974; Bhattacharya & van den Heuvel, 1991).

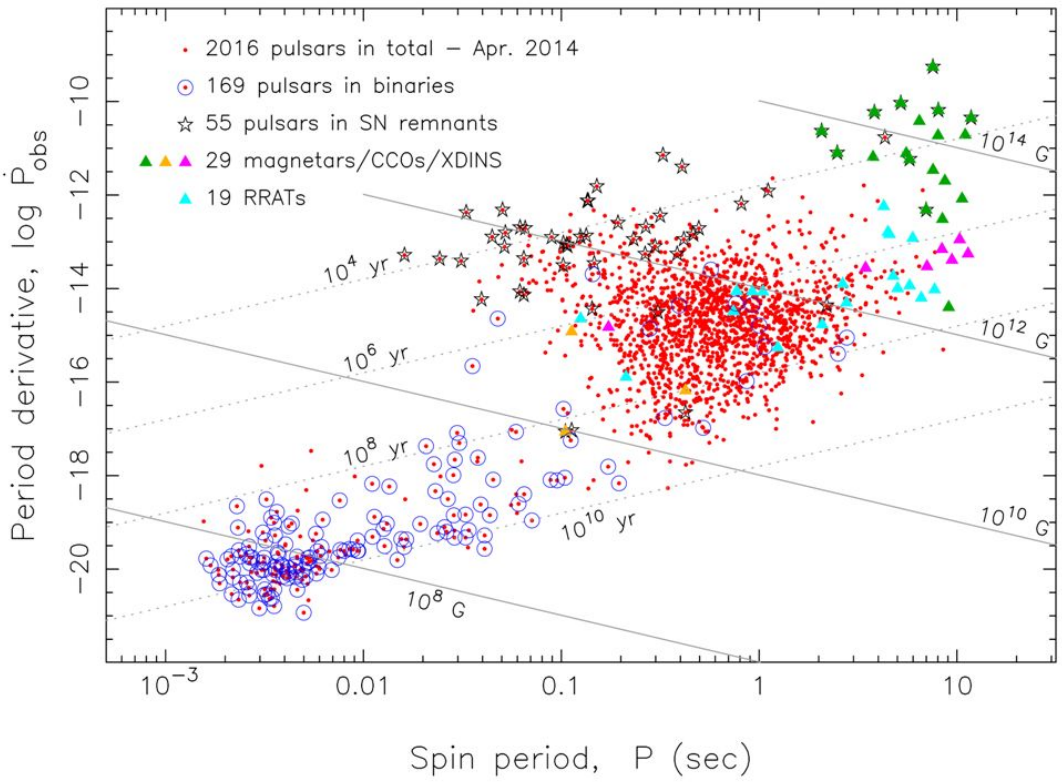

Figure 1.1: Period-Period derivative plane (Tauris et al., 2014) showing the distribution and groups of pulsars. Notice that almost all millisecond pulsars are in binary systems. The figure also shows lines of equal characteristic ages (dotted) and equal magnetic field strengths (solid). Another line of constant spin-down power (not shown) of about 10^{30}erg s^{-1} marks the graveyard boundary beyond which pulsars are no longer detectable (compare with Lorimer & Kramer, 2005a).

With the growing number of discovered pulsars, it is not surprising that attention narrows down to "interesting" pulsars. Perhaps pulsars find their fame not only in their unique features but more importantly, in their astrophysical applications (see Lorimer & Kramer, 2005a, for details). It is naturally conceivable that highly stable pulsars can serve as clocks that might be an alternative to atomic clocks (Petit & Tavella, 1996). Besides, their periodic pulses with generally well defined shape provide an excellent basis for probing the interstellar medium, testing general relativity with binary pulsars, and gaining insight into

plasma physics in extreme conditions by their emissions. In addition, they are "celestial laboratories" for studying interiors of stars. However, success in these applications largely depends on the theoretical description of the physics underlying the pulsar phenomenon and sufficient characterisation of pulsar features, especially spin periods and their time derivatives, to very high precision.

1.2 Period-dependent Properties of Pulsars

Estimates of some properties of pulsars can be obtained from the spin period. Assuming the pulsars are spinning magnetic dipoles and neglecting wind of out-flowing charged particles, which is also dependent on the rotational kinetic energy, we can write

$$\dot{E}_{rad} = \dot{E}_{rot}, \tag{1.1}$$

where $\dot{E}_{rot}$ is the rate of loss of rotational kinetic energy, often known as *spin-down luminousity* or *spin-down power* and $\dot{E}_{rad}$ is the power of radiation.

1.2.1 Braking Index

According to classical electrodynamics, the radiation power of a rotating magnetic dipole is given as

$$\dot{E}_{rad} = \frac{2}{3c^3}|\mathbf{m}|^2\omega^4 \sin^2\alpha, \tag{1.2}$$

where c is the speed of light, $|\mathbf{m}|$ is the magnetic dipole moment, ω is the rotational angular frequency and α is the angle of inclination between the rotation axis and the magnetic axis. The spin-down power is the derivative of the rotational kinetic energy:

$$\dot{E}_{rot} = -4\pi^2 I \nu \dot{\nu}, \tag{1.3}$$

where I is the moment of inertia of a solid, spherical pulsar and ν is the spin frequency. Substituting Equations 1.2 and 1.3 into Equation 1.1 and rearranging gives

$$\dot{\nu} = -\left(\frac{8\pi^2 |\mathbf{m}|^2 sin^2\alpha}{3Ic^3}\right)\nu^3, \tag{1.4}$$

which we can compare to a more general power law for spin-down

$$\dot{\nu} = -K\nu^n, \tag{1.5}$$

where K is a constant and the parameter n is known as the *braking index*.

In a vacuum condition where radiation emission is the exclusive consequence of the pulsar braking, the braking index $n = 3$ as expected from Equation 1.4. If $n \geq 3$, this would indicate that there may be other contributions to the spin-down which may be due to, among other things, the torque due to the particles lost along the magnetic field lines. The braking index n can be expressed in terms of the spin frequency and its first and second derivatives as

$$n = \frac{\nu\ddot{\nu}}{\dot{\nu}}, \tag{1.6}$$

after differentiating Equation 1.5. Hence the braking index can be evaluated given the spin frequency and its first two derivatives.

1.2.2 Magnetic Fields

As already mentioned in §2.1, a plausible explanation for the origin of the strong magnetic fields of pulsars is the conservation of the magnetic flux from their main sequence progenitor stars. Using the relation for the magnetic flux, $\Phi = \int \vec{B}.\vec{n}\,da$, where $\vec{n}$ is the unit vector normal to the area a intercepting the flux, shrinking to a much smaller size results in a tremendous increase in magnetic field strength to 10^{10} G; this is the typical factor by which the cross-sectional area reduces. This agrees with estimated values from the detection of cyclotron absorption features in X-ray binary spectra observations, which allows for the estimation of the surface magnetic fields of pulsars (see, for example Bignami et al., 2003). Estimates of magnetic fields from these observations range between $10^{11} - 10^{12}$ G.

An indirect way to estimate the magnetic field strength is to use the magnetic dipole analogy of Larmor's formula for the radiation energy of a rotating dipole in Equation 1.2. According to classical electrodynamics, $|\mathbf{m}| \approx BR^3$ (for example see Jackson, 1962). Substituting into Equation 1.2 and rearranging, it gives (assuming $R = 10\,\mathrm{km}$, and $I = 10^{38}\,\mathrm{kg\,m^2}$)

$$B_s = \sqrt{\frac{3c^3 IP\dot{P}}{8\pi^2 R^6 \sin^2\alpha}} \approx 10^{19}\sqrt{P\dot{P}}\ \mathrm{G}, \tag{1.7}$$

where $P = \dfrac{2\pi}{\nu}$ is the spin period, B_s is the surface magnetic field strength, R is the radius of the pulsar and I is the moment of inertia. This shows that B_s depends on the period of rotation P and $\dot{P}$, which can be determined by timing measurements. Again, this holds on the assumption that conversion to radiation is the only process by which spin-down power is lost.

1.2.3 Characteristic Age

Rearranging equation 1.7, it is found that

$$\begin{aligned} P\dot{P} &= P\frac{dP}{dt} \\ &= B^2\left(\frac{8\pi^2 R^6 \sin^2\alpha}{3c^3 I}\right) \\ &= K, \end{aligned} \tag{1.8}$$

a constant. Integrating Equation 1.8 over the life time, τ, of the pulsar;

$$\int_{P_0}^{P} P dP = K\int_0^{\tau} dt.$$

$$\tau = \frac{P^2 - P_0^2}{2P\dot{P}}$$

where $P_0 = P(t=0)$ or the period at birth. P_0 is usually unknown. However, until a reliable estimate of the initial spin period is found, the assumption $P \gg P_0$ is most reasonable. Hence the characteristic age, τ, is estimated as

$$\tau \approx \frac{P}{2\dot{P}}\,. \tag{1.9}$$

Here again, one notices that τ is dependent on the rotational period P of the pulsar. Nevertheless, its accuracy is compromised by two assumptions: (1) spin-down is due entirely to rotating magnetic dipole (i.e braking index $n = 3$) and (2) we can neglect the initial spin period at birth, P_0.

1.3 Pulsar Timing

Pulsar timing is the technique for determining the absolute time of arrival of every pulse with respect to the pulsar's inertial reference frame. Precise timing of the pulses allows the study of rich astronomical phenomena, including the interstellar medium and the detection of gravitational waves (eg. Demorest et al., 2012). During observation, local time stamps are given to the data, usually by a standard clock (caesium or hydrogen maser) at the observatory, synchronised with a Global Positioning System based time. The aim of pulsar timing is to transform the time stamp to the pulsar's inertial reference frame.

1.3.1 Initial Parameters on Discovery

The discovery of pulsars comes with the initial estimate of spin frequency and its derivatives as well as the astrometric parameters that are subsequently optimised. Interaction with a relatively homogeneous ionised electron plasma causes it to be frequency dispersed, i.e. the otherwise narrow pulse is broadened. This effect arises because high frequencies arrive earlier than the lower frequencies. The relative delay is quantified by the dispersion measure DM=$\int_0^d n_e dl$, where n_e is the free electron density along the line of sight and d is the distance between the observer and the pulsar.

Data is folded at the initially estimated period for the desired integration time. The pulse phase drift during the integration time is a reflection of a deviation of the initially estimated period P_{est} from the true period. The error is estimated by averaging the accumulated phase drift over the integration time (t_{int}) or the length of the data set. A better period P can then be obtained from the expression

$$P = P_{est} + P_{error} = P_{est}\left(1 + \frac{\Delta\phi}{t_{int}}\right), \tag{1.10}$$

where $\Delta\phi$ is the maximum phase drift in seconds over the entire integrated time. Similarly, the data set is folded with the initial DM across frequency channels. Any error in the estimated DM shows the need to improve its accuracy. This can be obtained given the time lag Δt (in seconds) over the observing bandwidth Δf:

$$\mathrm{DM} = \mathrm{DM}_{est} + 1.21 \times 10^{-4} \left(\frac{\Delta f^3}{f} \right) \Delta t, \tag{1.11}$$

where f is the centre frequency, also in MHz (Lorimer & Kramer, 2005a). Using the improved period and DM as estimates, much better values can be achieved by refolding the data following the above described steps again, or with freshly observed data. Doing so with longer t_{obs} ensures sufficient phase drift for accuracy. In most cases, the new period and DM are accurate enough for the next steps to proceed.

1.3.2 Standard Template

The next step in pulsar timing is aimed at finding the time difference by which the pulses are offset from their times of arrival (TOAs). The idea is to determine, with respect to the solar system barycentre, the TOA of a pulse so that together with the precisely measured period of the pulses, the retrospective TOAs of observed pulses can be determined and that of yet to arrive pulses can be predicted. This way, the number of pulses arriving between any two TOAs can additionally be computed; in other words, we are able to account for every rotation of the pulsar. This is achieved by matching an integrated pulse profile and a standard profile or template.

As indicated by Taylor (1992), a recorded sampled time-domain pulse profile $p(t)$ is made up of a scaled (by b) and shifted (by τ) intrinsic pulse profile, $\mathcal{T}(t)$ of the pulsar,

and uncorrelated white noise $n(t)$, expressed as

$$p(t) = a + b\mathcal{T}(t-\tau) + n(t), \tag{1.12}$$

where a is the constant off-pulse level.

The integrated pulse profile is obtained by averaging phase coherently added pulse profiles obtained during the observation at the best optimised period. A template is considered to be an ideal noise free representation of the intrinsic pulse, $\mathcal{T}(t)$, from the pulsar. The off-pulse region is set to a constant level (usually zero). Even though averaging a sufficiently large number of coherent pulses reduces the uncorrelated noise and produces a stable profile, fitting sums of Gaussian functions are suitable for creating a template (Foster et al., 1991; Kramer et al., 1994; Kramer, 1994). The latter method is represented mathematically for k components as

$$\mathcal{T}(t) = \sum_{i=1}^{k} h_i \exp^{-(\frac{t-\phi_i}{\sigma_i})}, \tag{1.13}$$

where h_i, ϕ_i and σ_i are the amplitude, the phase of the peak and the width at half maximum of the ith component respectively. The sums of Gaussian components produces a template with very high signal-to-noise ratio (S/N) and allows the flexibility of reproducing the template with any number of phase bins. Also, the amplitudes and widths of the Gaussian components can be adjusted to give phase aligned templates for profiles observed at nearby frequencies.

Closely related to the Gaussian function is the von Mises function. It is the circular analogue of the normal distribution function. It is defined for a range of values that represent a complete cycle. Similar to the sum of the Gaussian components, the template can

be described as the sum of the von Mises functions as

$$\mathcal{T}(t) = \sum_{i=1}^{\kappa} \frac{\exp^{\kappa_i \cos(t-\phi_i)}}{2\pi I_0(\kappa_i)}, \tag{1.14}$$

where κ_i is the shape parameter of the ith component and ϕ_i is the phase bin of the the peak of the ith component.

Generally as more components are added, the resultant template will better describe the ideal profile. However, including fine components may result in over-fitting. In other words the finer components may describe noise instead of improving the accuracy of the template. Normally, the template is compared to a high S/N profile and the χ^2-value of the residuals determines how well the template approximates to the intrinsic pulse profile. The optimum number of components for a given pulse profile depends on the shape, the S/N and the desired χ^2-value.

1.3.3 Determining the Pulse Time of Arrival

A typical pulsar observation consist of a number of pulses contaminated with noise and show significant pulse-to-pulse variations. Since high S/N is crucial to the TOA precision (see §1.3.4), several contiguous pulses (usually thousands) in an observation are coherently averaged in phase to obtain integrated pulse profiles with sufficient S/N and stable shapes. However, the times of arrival of the resulting integrated pulses are generally offset in phase from the observation time stamp. By setting the fiducial point of the template to the observation time stamp, for example, a cross-correlation between $p(t)$ and $\mathcal{T}(t)$, from Equation 1.12, produces a measure of the lag, or time offset τ between the fiducial phase of the template and that of the observed profile. The topocentric TOA, recorded at the observatory is the observation time calculated using the phase offset:

$$TOA_{topo} = t_{obs} + mP + \tau, \tag{1.15}$$

where m is a positive integer and P is the pulse period.

Since the topocentric TOA is subject to the Earth's rotation and orbit around the Sun, it is transformed to the more stable centre of mass of the solar system, also known as the solar system barycentre reference frame. The transformation relation is given by

$$TOA_{ssb} = TOA_{topo} + t_{corr} - DM/f^2 + R_{\odot} + S_{\odot} + E_{\odot} + R_{bin} + S_{bin} + E_{bin}, \tag{1.16}$$

where TOA_{ssb} is the transformed barycentre TOA, t_{corr} is the time corrections to the clock at the observatory to bring it to the International Atomic Time (TAI), $\frac{DM}{f^2}$ is the correction for the delay associated with frequency dispersion by the interstellar medium at the observation frequency f, $R_{\odot}$ is the Roemer delay which is the classical light travel time between the solar system barycentre to the telescope, $S_{\odot}$ is the Shapiro delay correcting for the effect of space-time curvature in the solar system, and $E_{\odot}$ is the Einstein delay correction for the total effect of gravitational redshift due to the other bodies in the solar system and time dilation arising from the motion of the Earth. The last three terms are the analogous Roemer, Shapiro and Einstein delays respectively, due to the pulsar's binary system if any.

The TOA_{ssb} transformation in Equation 1.16 sufficiently corresponds to the pulse rate of the pulsar, provided no relative motion exists between the pulsar and the solar system barycentre. The set of TOA_{ssb} is then fitted with a model that predicts the TOA_{ssb}. The model is expressed in terms of the instantaneous spin frequency $\nu(t)$, relative to an epoch

(reference time) t_0 in the form of a Taylor's series:

$$\nu(t) = \nu_0 + \dot{\nu}(t - t_0) + \frac{\ddot{\nu}(t - t_0)^2}{2!}..., \tag{1.17}$$

where $\nu_0 = \nu(t_0)$. Similarly, in terms of the phase evolution $\phi(t)$,

$$\phi(t) = \phi_0 + \nu(t - t_0) + \dot{\nu}(t - t_0)^2 + \frac{\ddot{\nu}(t - t_0)^3}{2!}..., \tag{1.18}$$

where $\phi_0 = \phi(t_0)$. Since $\nu(t) = \frac{\Delta N}{\Delta t}$, where ΔN is the number of pulses observed in the time interval Δt, the pulse number at predicted TOA, t after a reference TOA t_0 is the time integral of $\nu(t)$, given by:

$$N = \nu_0(t - t_0) + \frac{\dot{\nu}(t - t_0)^2}{2!} + \frac{\ddot{\nu}(t - t_0)^3}{3!} + ... \tag{1.19}$$

For perfect timing, N is an integer. The model predicts when the pulses are expected to arrive. The timing residuals,

$$R = TOA_{ssb} - TOA_{model}, \tag{1.20}$$

therefore reflect the deviation of the model from observation.

The goodness-of-fit is determined by taking the χ^2 value of the residuals. In order to compare values, the reduced χ^2 value is preferable. It is expressed as

$$\chi^2_r = \frac{1}{\mathrm{DoF}} \sum_i^{N_{TOA}} \frac{R_i}{\sigma_i}, \tag{1.21}$$

where N_{TOA} is the number of TOAs, σ_i is the uncertainty associated with the ith TOA and DoF (the number of degrees of freedom) is the difference between the number of

TOAs and the number of parameters fitted. It is desired that the χ^2 value of the fitting is minimised. This may require adjustment to some of the TOA corrections (e.g., dispersion measure) or the model (e.g., the derivatives of the spin parameters). A successful timing model results in the random distribution of the post-fit residuals with a mean of zero and its root-mean-square (RMS) equal to the mean TOA error.

Most of the timing procedure described above is incorporated into software packages such as PSRTIME[2], TEMPO2[3] and TIMAPR[4]. The packages use the ephemeris, astrometric parameters (i.e. position, proper motion and parallax), spin parameters (i.e. spin frequency and its derivatives) and binary parameters (e.g., orbital period and eccentricity), as well as the set of TOAs.

1.3.4 Precision in the Time of Arrival (TOA)

Apart from the corrections discussed earlier, other factors contribute to TOA precision. In the first place, the fiducial point corresponding to the TOA is only detectable when it is well above the noise level. In other words, the uncertainty in the TOA is inversely proportional to the signal-to-noise ratio ($\sigma_{TOA} \propto \frac{1}{S/N}$). However, the radiometer equation leads to

$$\mathrm{S/N} = \sqrt{n_p t_{obs} \Delta f} \left(\frac{S_{mean}}{S_{sys}} \right) \frac{\sqrt{W(P-W)}}{P} \tag{1.22}$$

where n_p is the number of polarisations, t_{obs} is the integration/observation time, Δf is the observation frequency bandwidth, S_{sys} and S_{mean} are the system and mean flux densities, respectively, W and P are pulse width and period respectively (see Lorimer & Kramer,

[2]Jodrell Bank Observatory
[3]Austrsalian Telescope National Facility/Princeton University
[4]Pushchino Observatory/Max-Plank Institute for Radio Astronomy

2005a, for details). It follows that

$$\sigma_{TOA} \propto \frac{P}{\sqrt{n_p t_{obs} \Delta f}} \left(\frac{W}{P}\right)^{\frac{3}{2}} \times \frac{S_{sys}}{S_{mean}} \,. \tag{1.23}$$

Hence errors in the TOA reduce with longer observation time, larger bandwidth, minimised system noise, and narrow pulses.

1.3.5 Physical Quantities Obtained from Timing Residuals

The distribution of the timing residuals from a data set covering long time-scale may reveal structures that represent effects that were not accounted for, or incorrectly included in the basic timing procedure. A few examples of these structures are demonstrated in Figure 1.2. The best timing result is indicated by the random Gaussian distribution of the residuals with zero mean (Figure 1.2a). The distribution of the residuals reflect the inevitable effects on the propagation of the pulses such as noise, scattering, pulse shape evolution and spin irregularities. A parabolic rise in addition to a random residual distribution as in Figure 1.2b indicates an error in the period derivative. A sinusoidal structure as seen in Figure 1.2c becomes obvious when the position is incorrect.

If the motion of the pulsar, relative to the solar system barycentre, is neglected in the timing correction, additional time dependent terms are added to the residuals. For example, transverse motion adds a linear time term and can be evaluated if not known a priori (Figures 1.2c). However, the Doppler effect on the pulses due to radial velocity are absorbed into the pulse period and cannot in general be determined from timing analysis.

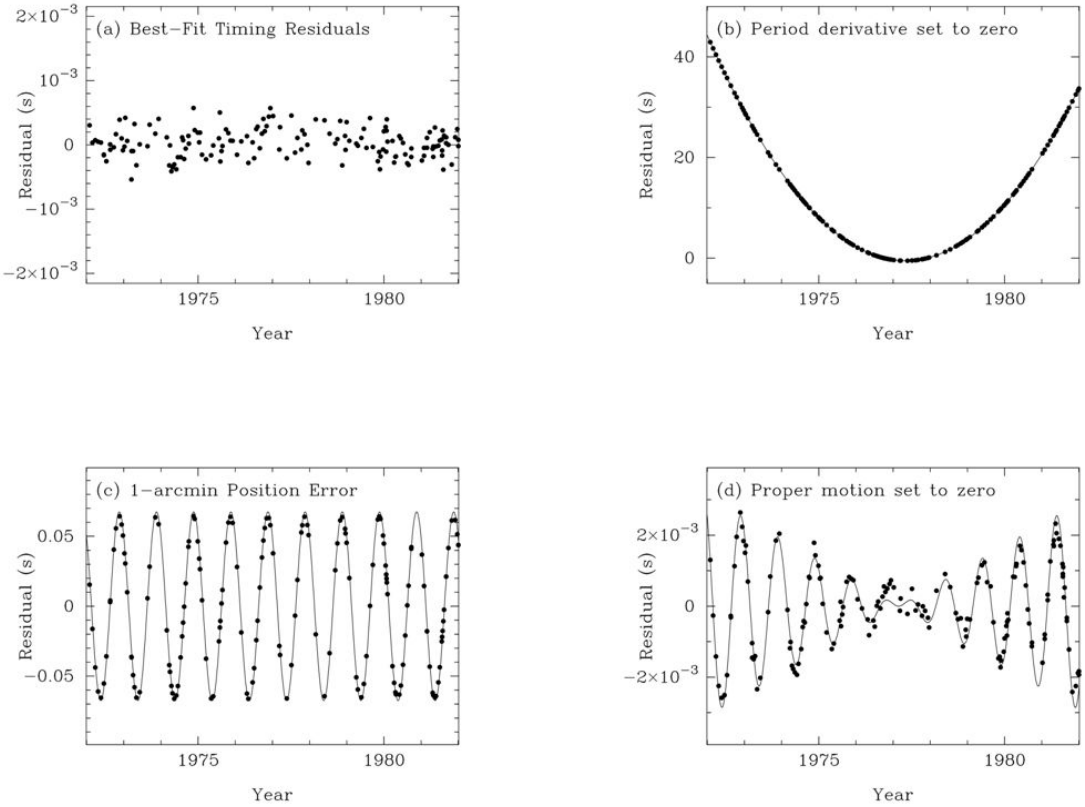

Figure 1.2: Some post-fit residual distributions with systematic variation and their implications (Lorimer, 2001): (a) A perfect timing analysis results in randomly distributed residuals with zero mean; (b) An incorrect period derivative shows as parabolic structure; (c) a sinusoidal residual distribution indicates error in the position of the pulsar; and (d) modulated sinusoidal variation is a reflection of unaccounted-for proper motion of the pulsar in the timing model.

1.3.6 Timing Noise

If the TOAs are ideally corrected and the timing model perfectly describes the spin characteristics of the pulsar, the timing residuals will have a normal distribution with a mean of zero and standard deviation that reflects TOA measurement errors. This is typically the case on relatively short time-scales (e.g. days). However, residuals of some pulsars reveal significant structure indicating *timing irregularities* of the pulsar, usually on longer time-scales such as years. There are two main categories of timing irregularities: glitches

and timing noise. While a brief descriptions of both timing irregularities are given in the next few paragraphs, much of this work is linked to timing noise.

A glitch is a sudden step change in spin frequency (typical magnitude of $\frac{\Delta\nu}{\nu} \approx 10^{-9} - 10^{-6}$) and is often accompanied by a step change in the frequency derivative ($\frac{\Delta\dot{\nu}}{\dot{\nu}} \approx 10^{-3} - 10^{-2}\,\mathrm{Hz\,s^{-1}}$) (e.g. Lin & Zhang, 2004). This short event is sometimes followed by a quasi-exponential decay of the post-glitch spin frequency towards the pre-glitch value. A glitch in the Crab pulsar is shown in Figure 1.3.

Since the first observation of glitches in the Crab and Vela pulsars (Boynton et al., 1969; Radhakrishnan & Manchester, 1969), glitches have been reported in relatively few pulsars (e.g. Shemar & Lyne, 1996; Wang et al., 2000; Krawczyk et al., 2003; Espinoza et al., 2011). Glitches are more pronounced in younger normal pulsars, such as the Crab and the Vela pulsars (e.g Lyne et al., 1995). A popular interpretation of glitches and its characteristic recovery curve is the presence of superfluid enclosed in a rigid crust (Ruderman, 1969). A sudden transfer of angular momentum from the faster interior superfluid to the crust causes a jump in the spin frequency.

Unlike glitches, timing noise is fairly continuous with a low frequency spectrum. Irregular structures in the timing residuals are considered timing noise after all applicable corrections to the TOAs have been applied and the best model is used to fit the TOAs (see Figure 1.4 for sample timing noises). Timing noise thus represents effects of the pulsar's dynamics and/or emission mechanism that are not yet understood and are thus not included in the timing model.

Timing noise is common to most pulsars (Hobbs et al., 2010b). Early suggestions to explain timing noise included random walk processes involving unresolvable step functions in either the phase, spin frequency or its derivative (e.g. Cordes & Helfand, 1980),

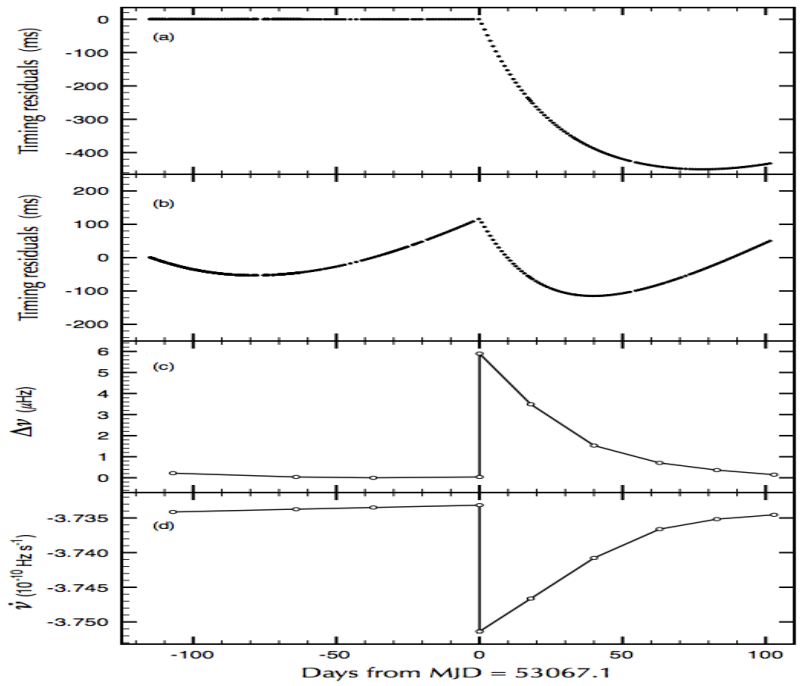

Figure 1.3: A small glitch in the PSR B0531+21 (the Crab) which occurred some time around MJD 53067 (Espinoza et al., 2011). The residuals when the model is fitted (a) up to the glitch event and (b) entire data set in the plot. The corresponding changes in the spin frequency, ν, and spin-down rate, $\dot{\nu}$, are shown in (c) and (d) respectively. The fractional step increase in frequency was 5.33×10^{-9}.

the existence of companion planets that are not considered in the timing model (e.g. Demiański & Prószyński, 1979), and free precession whereby the spin axis is not perfectly aligned with the angular momentum vector, resulting in the spin axis itself rotating about the angular momentum vector (e.g. Stairs et al., 2000). Residual structure attributed to free precession is expected to be periodic and the pulse shape would vary with the same periodicity. However, in a study of the timing noise of 366 pulsars, Hobbs et al. (2010b) ruled out some earlier postulates that seek to explain the possible origins of timing noise. For example, the same timing noise features were seen in data of the same source from

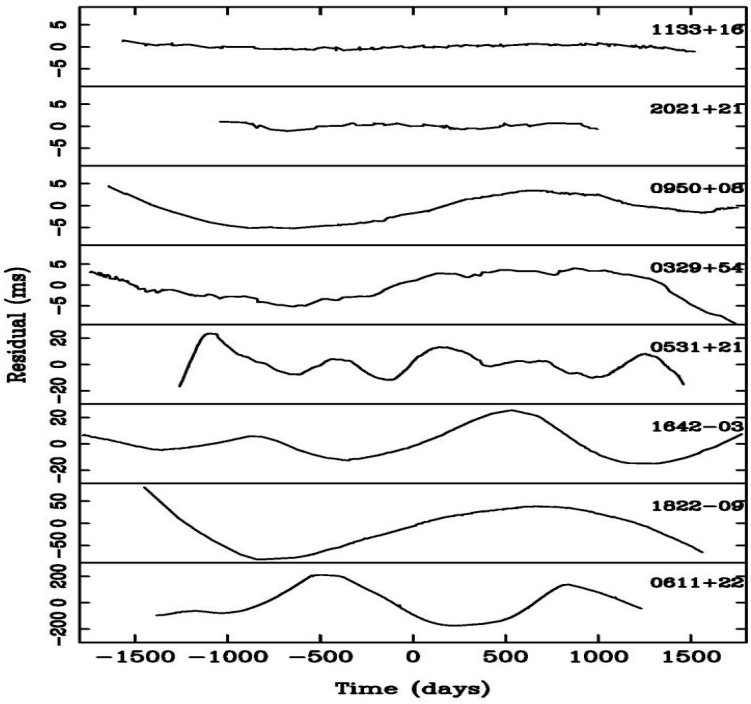

Figure 1.4: Examples of timing noise of 8 pulsars over a time span of 8 years (Lyne, 1999).

different observatories. This showed that timing noise could not be caused by the observational set-up. They also compared the residuals of the same data sets using different timing packages and found that timing noise was not caused by off-line timing processing. Similar timing noise in data taken at different observing frequencies allowed for an association between timing noise and interstellar or interplanetary dispersion to be ruled out. Other conclusions from their research were that the structure in the timing noise varied with time span of the data, and that post-glitch recovery is a possible cause of timing noise.

It has been observed that the timing noise varies with increasing time span of data as well as the order of polynomial function that needs to be fitted to the TOAs. In order to

quantify the level of timing noise for a given pulsar, Cordes & Helfand (1980) defined an *activity parameter*, A, as the common logarithm of the ratio of the root mean square of the residual phase of the pulsar ($r(m,T)_{pulsar}$) to that of the Crab pulsar ($r(m,T)_{Crab}$, considered as a standard) over equal time span of data (T in days) and fitted with the same order of polynomial (m), i.e.

$$A = \log\left(\frac{r(m,T)_{pulsar}}{r(m,T)_{Crab}}\right). \tag{1.24}$$

Arzoumanian et al. (1994) instead defined a *stability parameter* as

$$\Delta(T) = \log\left(\frac{|\ddot{\nu}|T^3}{6\nu}\right) \tag{1.25}$$

for $|\ddot{\nu}|$ greater than twice the value of its uncertainty $\sigma_{\ddot{\nu}}$, and an upper limit

$$\Delta(T) < \log\left(\frac{2\sigma_{\ddot{\nu}}T^3}{6\nu}\right) \tag{1.26}$$

otherwise. Using these timing noise variation parameters in independent studies, the authors came to a common conclusion; a correlation exists between the timing noise level and the spin-down rate.

Despite the noise in their timing residuals, pulsars are famed for their highly precise emission of periodic pulses that is in phase coherence with their spinning. Their importance lies partly in the precision of the spin frequency. In this, the millisecond pulsars become more useful, with their much reduced timing irregularities. For example, the coalescing of supermasive binary black holes induces a gravitational wave signature that would introduce an amplitude of approximately 10 ns in the timing residuals of a pulsar

(Hobbs et al., 2010a). Hence, the Pulsar Timing Array (PTA) project, currently being developed to detect gravitational waves, requires millisecond pulsars whose intrinsic timing noise is about the same level as 10 ns for accurate measurement of gravitational waves. On the other hand, normal pulsars spin irregularly, and as this is reflected in their timing, its noise can provide clues to the interior structure of the pulsar and / or other objects in the neighbourhood of the pulsar (Haskell & Melatos, 2015). Hence, a complete unified explanation for the causes of timing noise, and a full understanding of it will allow appropriate constraints in the studies involving the use of pulsars.

1.4 Organisation of the Thesis

As indicated in the preceding section, understanding the physical processes underlying timing noise is an important step towards their application to gravitational wave detection. The aim of this research is to investigate some characteristic features of the timing noise of PSR B0329+54. In chapter 2, the physical processes underlying pulsar emission and some available literature on PSR B0329+54 will be reviewed. In chapter 3, the observation data on the pulsar as well as the preparation of the data, including machine learning classification into the two profile modes of the pulsar, will be described. This will lead to the analysis and interpretation of results in chapter 4 before concluding in chapter 5.

Chapter 2

Physics of Pulsar Emission

An exotic astronomical object such as pulsar, with its stable moment of inertia in vacuum, is expected to maintain stable rotation. The changes and different physical conditions within and around the neutron star can affect this ideal state. As a magnetic dipole, the pulsar radiates electromagnetic waves according to the Larmor' principle (see § 1.2). However, the radiation power estimated from observation is found to be just a fraction (approximately 10^{-9}) of the loss of rotational kinetic power (e.g, Gunn & Ostriker, 1969; Timokhin, 2010; Hermsen et al., 2013). Moreover, it is believed that the additional braking torque on the pulsar is introduced by the flow of high energy charged particles (e.g Kramer et al., 2006; Goldreich & Julian, 1969). Understanding how these mechanisms affect the spin parameters of pulsars would provide valuable insight into the causes of timing noise and the emission process.

2.1 The Pulsar Magnetosphere

Pulsars are known to have strong magnetic fields, between 10^8 and 10^{14} G. While this strong magnetic field has little effect on the interior processes of the neutron star (Ruderman, 1974), all exterior physical processes are dominated by the magnetic field (Lyne & Graham-Smith, 2005).

A number of theories have been proposed to describe the surface and surroundings, as well as to explain how the radiation is emitted from the pulsar. While each theory on its own merit explains some pulsar phenomena well, a conclusive and unified description and explanation are yet to be found (e.g. Melrose, 1995). For example in the earliest attempt to model radio emission by Goldreich & Julian (1969), a simplified model in which the rotation and magnetic axes were aligned was assumed. In this picture, an external electric field drives charged particles from the stellar surface along the magnetic field lines as the Lorentz force overcomes the gravitational force on charged particles. This model could not successfully be extended more generally to a pulsar with an inclined magnetic axis, which accounts for its lighthouse behaviour, but it provides the basis for understanding the emission processes of pulsars (Mestel, 1971).

As shown in Figure 2.1, an imaginary cylindrical boundary is defined such that any point within the boundary co-rotating with the pulsar does not exceed the speed of light. This is known as the light cylinder, with radius $R_{LC} = \frac{cP}{2\pi}$, where P is the pulse period and c is the speed of light. The magnetic field lines that close within the light cylinder are referred to as closed field lines and those that intercept the light cylinder are the open field lines. The magnetosphere is therefore the atmosphere within the light cylinder filled with highly energetic plasma and dominated by the strong magnetic field.

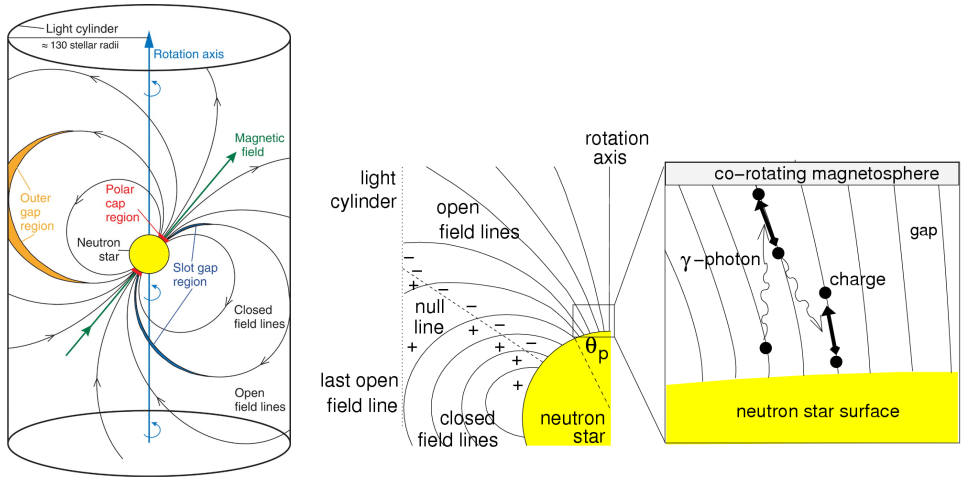

Figure 2.1: (a) A toy model of the pulsar and its magnetosphere (Aliu et al., 2008). The magnetosphere is bounded by the light cylinder, within which charged particles and structures co-rotate with the pulsar. The open field lines intercept the light cylinder and the closed field lines close within the light cylinder. (b) The mechanism of pair production (Lorimer & Kramer, 2005a). A zoomed-in section of the polar cap illustrates the pair production mechanism.

2.2 Radiation Emission Regions

In the aligned rotator model of Goldreich & Julian (1969) shown in Figure 2.2, the magnetosphere is the plasma-filled space around the pulsar enclosed by the light cylinder (see § 2.1). Critical field lines emerge from points on the stellar surface where the electric potential is the same as that of the interstellar medium. The model is comparable to a Faraday disc (e.g. Michel & Li, 1999); electric potential is highest at the equator and decreases with latitude towards the poles. Under these conditions, electrons flow along open lines at higher latitudes while the positrons follow along the open lines at lower latitudes.

Within the magnetosphere, the high-energy plasma co-rotates with the pulsar. However, the charged particles streaming along open field lines escape the magnetosphere with relativistic speeds. This causes the magnetic field lines to sweep back contributing

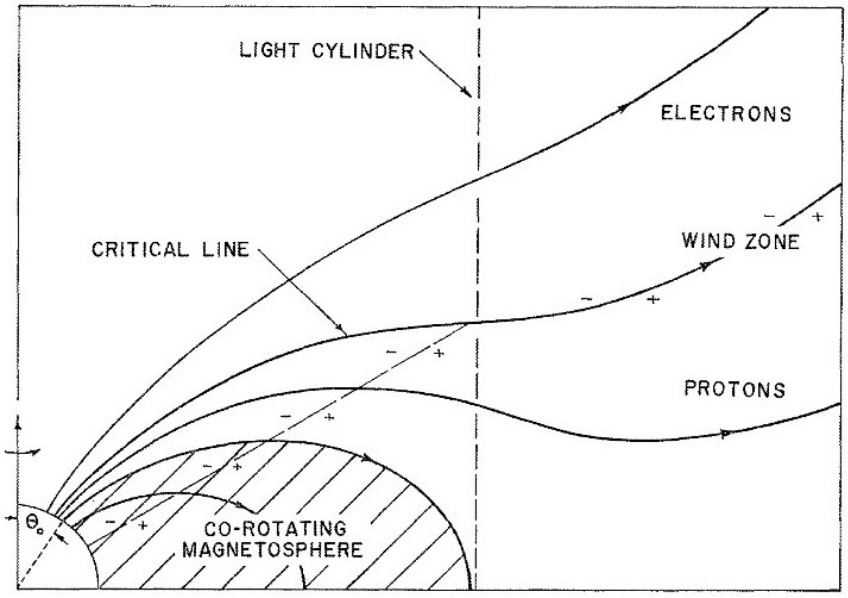

Figure 2.2: The axisymmetric model of the pulsar (Goldreich & Julian, 1969). The pulsar is located at the bottom left corner with rotation vector in the vertical direction. The shaded region bounded by the last closed magnetic field line is the plasma filled magnetosphere co-rotating with the pulsar.

to the torque on the pulsar. This simplified model can be used to illustrate possible regions where radiation is emitted, as well as the physical mechanisms that are involved. Two regions, collectively referred to as *acceleration gaps* are identified: the *polar cap* and the *outer gap* (e.g Lorimer & Kramer, 2005b).

The *polar cap* region is defined by the feet of the points where the closed magnetic field lines, tangential to the light cylinder emerge from the stellar surface. A given magnetic field line can be drawn using polar coordinate (r, θ) with the pulsar at the centre such that $\dfrac{\sin^2\theta}{r}$ is a constant. The circumference of the polar cap is bounded by the feet of the outermost closed field lines tangential to the light cylinder. Using the coordinates of the points at which a chosen outermost closed line intercept the stellar surface (R_s, θ_s) and touches the light cylinder (R_{LC}, θ_{LC}), leads to $\dfrac{\sin^2\theta_s}{R_s} = \dfrac{\sin^2\theta_{LC}}{R_{LC}}$. Hence, the angular

radius, θ_s, of the polar cap can be calculated from

$$\sin^2\theta_s = \frac{R_s}{R_{LC}} = \frac{2\pi R_s}{cP}, \tag{2.1}$$

since $\theta_{LC} = 90^0$ and $R_{LC} = \frac{cP}{2\pi}$. Given the typical values of pulsar radius of 10 km and a spin period of 1 s, the angular radius of the polar cap is approximately 1.44×10^{-2} degrees, equivalent to a radius of about 145 m.

Some inconsistencies between the observed pulsed emission in the high energy regime and the pulsed radio emission can be explained by the proposed outer gap model (Cheng et al., 1986; Romani, 1996; Takata et al., 2004; Hirotani, 2008). For example the velocity of particles responsible for the radio emissions in the polar cap region is not sufficient to generate gamma-rays in some pulsars such as the Vela and the Crab pulsars (Abdo et al., 2009, ; also see § 2.3). Also, the light curves of most gamma-ray pulsars show double peaks that are out of phase with the radio pulse. Moreover, the two gamma ray peaks are usually separated by 0.4 in phase. These observed characteristics indicate that the high-energy emissions originates from region on the stellar surface, the outer gap. The outer gap is the region bounded by the outermost closed lines, the open field lines and the null surface (Figure 2.1). The null surface satisfies the condition, $\omega\cdot\mathbf{B} = \mathbf{0}$, where ω is the angular frequency and the $\mathbf{B}$ is the magnetic field. In the outer gap, the relativistic particle depletion leaves an extended region separating surfaces of opposite charges.

2.3 Emission Mechanisms

Even though a self-consistent theory pulsar radio emission mechanism is yet to develop, the early works of Goldreich & Julian (1969), Mestel (1971), Sturrock (1971), Ruderman

& Sutherland (1975) and Arons & Scharlemann (1979) have been used to explain a number of the observed pulse features. Detailed review of these theories and new ideas can be found in Michel & Li (1999) and Beskin (2009). Here we provide a simple description of some features of the pulsar emission mechanism for the purpose of this work.

A very high electric potential of the order $10^{10} - 10^{15}$ Volts exists between the pulsar's magnetic poles and the equator due to the rapid rotation and the high magnetic field (Lyne & Graham-Smith, 2005). Within the closed field lines, the current of plasma flow from higher latitude is conducted to the equator. Hence plasma within the closed lines co-rotate with the pulsar. In the acceleration gaps, however, ionised particles are accelerated by the high electric potential along open field line and eventually escape into the interstellar medium. The acceleration of these ionised particles in the acceleration gaps are thought to be the sources of pulsar radiations for most radio pulsars.

A number of radiation processes come into play as the ionized particles move along the magnetic field lines (e.g. Beskin et al., 1988). At non-relativistic velocity, the particles spiralling around the magnetic field lose energy by radiating photons. The cyclotron radiation emitted by a particle moving with non-relativistic speed is monochromatic at the Larmor frequency. At relativistic velocity however, the radiation becomes synchrotronic. In synchrotron radiation, the frequency spectrum includes harmonics of the Larmor frequency. The number of harmonics increases with increasing relativistic factor so that the spectrum may be classified as continuous. At the polar cap where the field lines are highly concentrated, the ionised particles are constrained to move almost parallel to the the field lines (i.e. almost zero pitch angle). The transverse acceleration of the particle as it travels along the curved path results in curvature radiation (see Lorimer & Kramer, 2005a).

The observed brightness temperature of pulses is explained by a cascaded pair production mechanism in the polar caps, described as follows: a primary photon emitted in

the curvature process interacts with the adjacent field giving rise to an electron-positron pair. The pair travels along the field line in opposite directions (Figure 2.1b). As they do, they emit a secondary photon and the process repeats (see, for example, Xu & Qiao, 2001; Spitkovsky, 2004). This increases the number density of the plasma but the energy of the photons is reduced. At some stage the energy of the photons fall below twice the rest mass energy of an electron and the cascade ends (Lyne & Graham-Smith, 2005).

2.4 Pulsar Spin and Emission Irregularities

Pulsars naturally lose angular momentum over time, represented by the spin-down rate. The spin-down rate can be measured with remarkably high precision in a relatively short time scale but may show variations from the ideal behaviour. Also, individuals pulses may vary in pulse phase, pulse shape or both. These variations reflect the irregularities in the spin frequency and emission processes of the pulsar and they have been shown to contribute to timing noise – a setback to some pulsar applications such as the search for gravitational waves. Nevertheless, these irregularities are believed to hold clues to the physics of pulsars, such as the emission mechanism.

This section is concerned with the review of irregularities attributed to the radio emission of pulsars and their contribution to timing noise. This will be preceded by a brief discussion of the pulsar spin irregularities in order to distinguish them from emission irregularities. Pulse profile irregularity is the abrupt change in the pulse profile (i.e intensity, width and shape) between pulses of the same pulsar. These include nulling, mode changing and sub-pulse drift.

2.4.1 Pulse Nulling

Backer (1970) first defined nulling as the temporal "pulse energy decrease by a factor of ten or more" over at least a pulse period (Ritchings, 1976; Lorimer et al., 2012). In a study focused on PSR B1944 +17, Deich et al. (1986) defined a null state using a 5σ noise level threshold. A period is considered null if the flux density within a pulse window remained below the threshold. In some visual inspections of pulse sequence, weak pulses may be $\leq 1\%$ of average pulse energy (e.g. Biggs, 1992). Hence a null is undetectable or practically zero flux density. By this definition, nulling is used with respect to the pulse height or intensity.

A number of suggestions have been made to explain nulling. Backer (1970) initially attributed it to a perturbation in the magnetosphere either dumping or dispersing charges in the radiating regions. Nulling also fits within the emission reversal model (Melikidze & Gil, 2006), intermittent failure in the production of the charge pair mechanism due to old age (Biggs, 1992) and changes in magnetospheric current (Wang et al., 2007). The possibility of asteroidal debris from supernova entering the magnetosphere to perturb current flow and radiation has also been proposed (Cordes & Shannon, 2008). While explanations based on the emission mechanism in the magnetosphere are highly favoured, a combination of these suggestions give better explanation to nulling as well as other closely linked phenomena.

It is generally believed that nulling is not an isolated phenomenon. For example, Ritchings (1976) found that pulsars with longer pulse period had the tendency to null more (i.e high nulling fraction). Hence as the pulsar gets closer to the "death valley" along its evolutionary path in $P - \dot{P}$ space, nulling become more probable. This suggested that the emission mechanism breaks down with loss of magnetic field strength. Other studies

reported evidence of a significant relationship between nulling fraction and characteristic age (Biggs, 1992; Wang et al., 2007). These findings suggest that nulling is more likely to occur in older pulsars.

One can plausibly attribute pulsars' high nulling fractions to this behaviour. In this picture, one would expect rotating radio transients (RRAT) to be generally old pulsars, which occasionally emit when conditions for coherent emission are right (Biggs, 1992; Zhang et al., 2007; Keane et al., 2011). Other suggestions include weak or distant pulsars with high modulation indices (Keane et al., 2011) and asteroid belts (Cordes & Shannon, 2008).

2.4.2 Mode Changing

A more general form of pulse shape irregularity is mode changing or mode switching. This refers to the abrupt changes between two or more quasi-stable pulse shapes. Nulling can be considered as mode changing in which one mode has very low flux intensity (Esamdin et al., 2005). Recently, Li et al. (2012a) suggested that vacuum and plasma filled magnetospheres were two extremes in terms of electric conductivity in support of earlier suggestions that mode changing and nulling were different relics of the same event in the magnetosphere.

Lyne et al. (2010) showed that the pulse shape of some pulsars are also correlated or anti-correlated with the spin-down rate, $\dot{\nu}$. They compared the average pulse shape and the spin-down rate over the same time period for each of six pulsars they studied (Figure 2.3). Their results led to the conclusion that mode changing, as in nulling, was a magnetospheric phenomenon dependent on particle outflow through the magnetic poles – the same mechanism that drives pulsar spin-down (see §1.2.2). Also, the results showed

a strong linear relationship between the changes in spin-down rate ($\Delta\dot{\nu}$) and the pulse shape. Hence slowly varying timing noise component arising from variations in $\dot{\nu}$ may be corrected by tracking the changes in the shapes of pulses.

2.4.3 Intermittent Pulsars

Any pulsar behaviour in which a long period (months and years) in a null state is followed by a relatively short period (days) of successive pulses is termed intermittency. This behaviour was first reported by Kramer et al. (2006) for PSR B1931+24, which turns 'off' for 25–35 days and turns 'on' for 5–10 days in a quasi-periodic fashion. Within the time span of the observed data studied, it was discovered that two spin-down rates – one for each state – were required in the timing analysis, state instead of the average spin-down rate measured over the entire data set. Including this extra term resulted in the timing noise being reduced by 20%. A second intermittent pulsar, PSR J1841–0500, was reported as turning off after a year of discovery and turned on again after 580 days Camilo et al. (2012). In this later study, $\dot{P}$ in the on-state was 250% of that in the off-state. These results suggested that this class of pulsed emission reduces the spin-down rate and contributes to the timing noise (Lyne et al., 2010).

As in other forms of nulling, changes in the magnetosphere has been linked to intermittency. For example, it has been suggested that a global failure of magnetospheric current may account for these extreme forms of nulling (Lyne et al., 2010). Even though it is believed that extreme nulling in intermittency is another manifestation of variations in magnetospheric emission mechanism, it is difficult to arrive at a consistent and unified explanation. Frequent monitoring (high cadence) over longer time scale will likely provide further and better clues to explaining these phenomena.

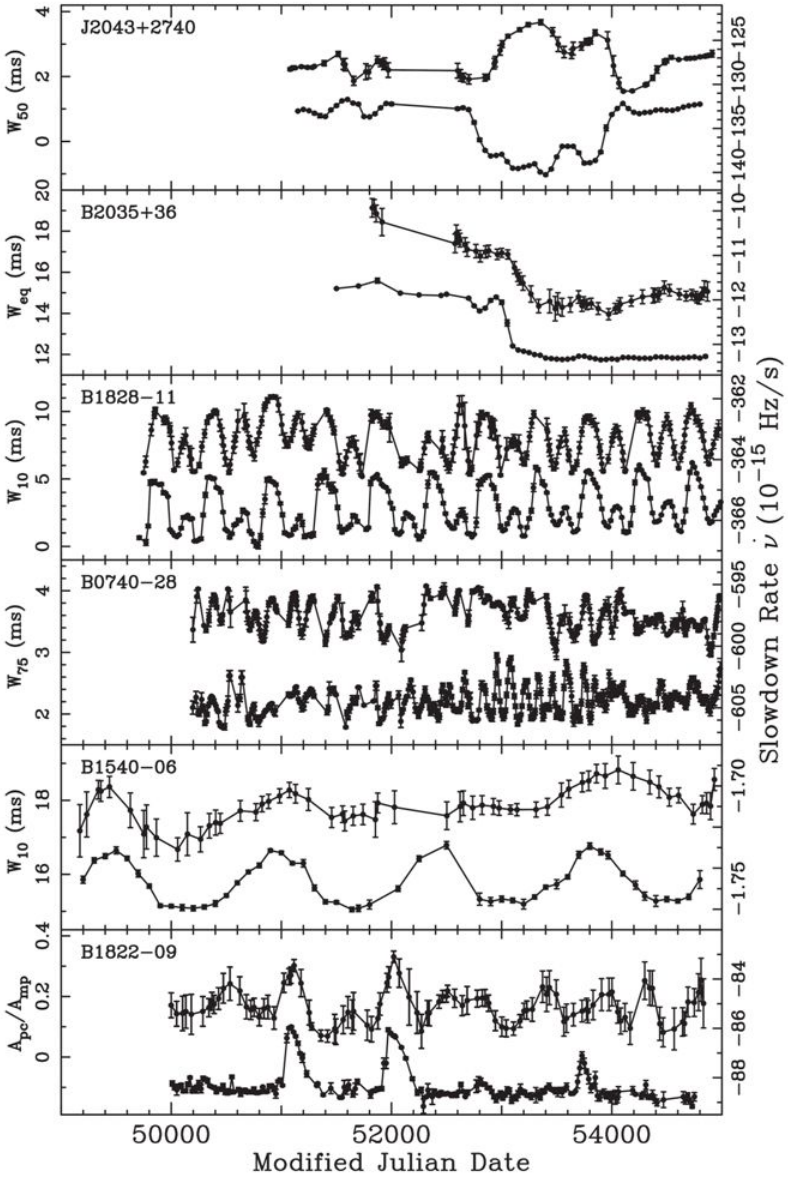

Figure 2.3: Pulse shape and spin-down rate for six pulsars compared. The upper and lower traces in each panel are respectively the pulse shape and spin-down rates. Correlation between the two parameters are clearly evident (Lyne et al., 2010).

2.5 Characteristics of PSR B0329+54

PSR B0329+54 belongs to the class of normal pulsars that make up most of the pulsar population. It was discovered in 1968 in Cambridge with a spin period of 0.714 s (Cole & Pilkington, 1968). Table 2.1 shows some properties of PSR B0329+54 obtained through timing observations. It is located at a parallax-determined distance of about 1.03 kpc at a Galactic longitude of 145^{o} and latitude of -1.2^{o} (Brisken et al., 2002; Popov et al., 2016). Known for nearly as long as pulsar astronomy, PSR B0329+54 has been studied extensively for a number of interesting features that it exhibits.

Perhaps the most important feature about this pulsar is its strong flux density across a wide frequency spectrum. Its average flux density of 203 mJy (at 1.4 GHz), makes it one of the brightest pulsars in the Northern sky (Brisken et al., 2002). Despite the general steep spectra characteristic of pulsars, PSR B0329+54 has been observed at 43 GHz, though the maximum flux density is possibly recorded around 300 MHz (Kramer et al., 1997; Kramer et al., 2003). This important feature allows detailed studies of its single pulses. For example, in a simultaneous single pulse observations of PSR B0329+54 over multiple frequencies, it was found that pulse intensities at different frequencies are correlated, corroborating earlier studies (Karastergiou et al., 2001, 2004).

In addition, it exhibits a number of typical pulsar phenomena that are still open to questions including mode changing over multiple frequencies (Lyne, 1971; Kramer et al., 1997) and multiple pulse components (see e.g Gangadhara & Gupta, 2001). The remainder of this chapter describes PSR B0329+54 in further detail. The aim is to review the key findings from the literature (§2.6, 2.7, 2.8).

Label	Value
Right Ascension ($\alpha_{J2000.0}$)	03:32:59.3862
Declination ($\delta_{J2000.0}$)	+54:34:43.5051
Spin Period (s)	0.714
Dispersion Measure	26.776
Proper motion μ_α (mas year^{-1})	17.00 ± 0.27
Proper motion μ_δ (mas year^{-1})	-9.48 ± 0.37

Table 2.1: Some properties of PSR B0329+54 (Brisken et al., 2002).

2.6 Components of the Pulse Profile

PSR B0329+54 is also famed for its multi-component pulse profile which provides insight into the emission geometry of pulsars. Hesse (1973), for example, had identified five components in the pulse profile. His results were based on the relative intensity of pulse profiles obtained by averaging 250 contiguous pulses observed at 2.695 GHz. Later, it was classified among "triple (T)" pulsars in the Rankin (1990) classification scheme for its clearly visible three peaks.

Another study by Kuzmin & Izvekova (1996) led to the proposal of a six-component model. They adopted the Gaussian fit separation of the average profile developed by Wu et al. (1998) to decompose the integrated pulse profiles into sums of Gaussian-shaped components. They found out that using six Gaussian components matched the profiles of PSR B0329+54 observed at multiple frequencies selected between 1 GHz - 10 GHz better than the five-component model. The sixth component was confirmed by Gangadhara &

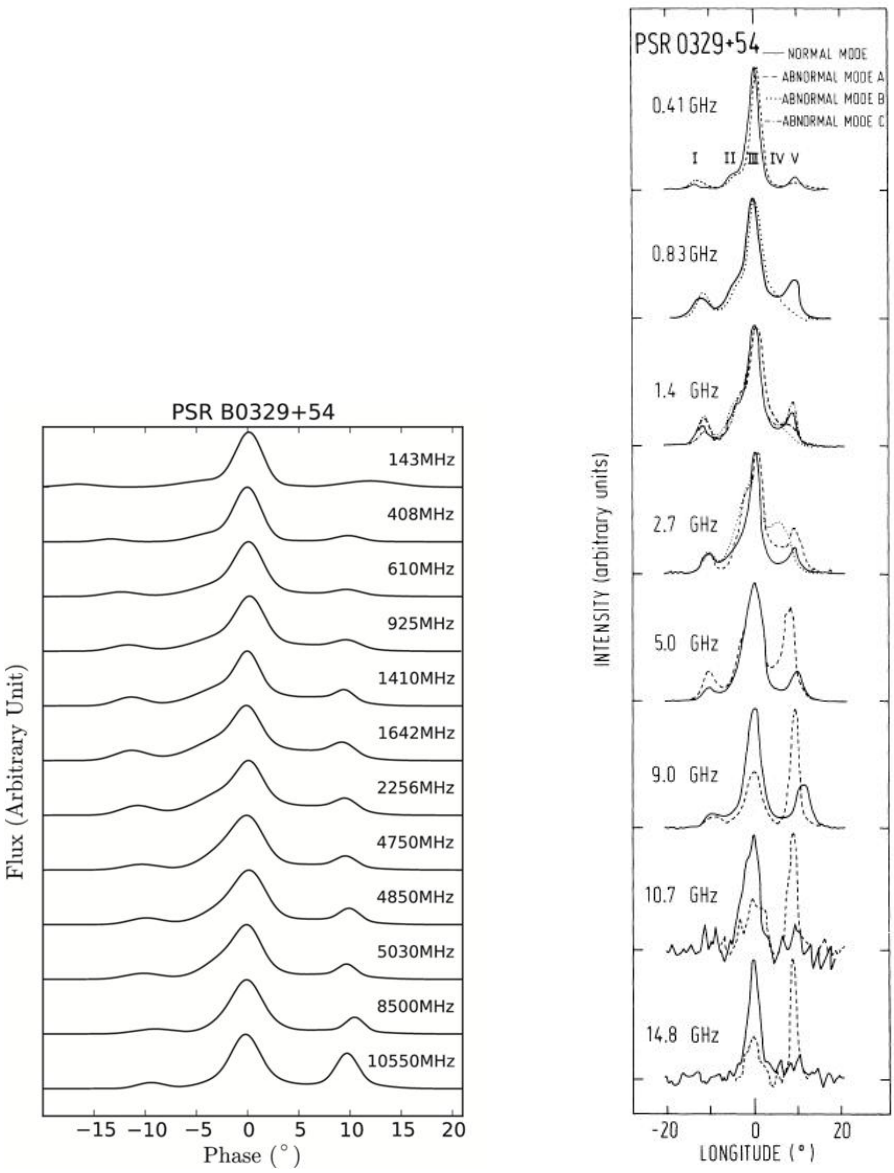

(a) **(b)**

Figure 2.4: The pulse profile components and the profile modes. The profiles in (a) were obtained by fitting sums of Gaussian-shape components to observed data (Shang et al., 2017) at eight different frequencies. Each profile was normalised with its maximum value. It can be seen that the trailing component increases in energy with increasing frequency while the separation among components narrows. In addition to the profile components, (b) shows mode changes at various frequencies (Bartel et al., 1982). The abnormal modes (indicated with different dashed lines) show wide variations, especially in the trailing component, over multiple frequencies.

Gupta (2001) using the so called "window-threshold" technique, designed to detect weak emission components (Gangadhara et al., 2000). In addition to the detection of the sixth component, they reported three more weak components, making a total of nine profile components reported for this pulsar.

Thus a typical pulse profile consists of a leading (I), a core (III) and a trailing component (V) (see the profile observed at 0.41 GHz in Figure 2.4b). The "saddle" component (II) on the rising edge of the main component is also significant. The intensity of the leading and the trailing components are respectively about 7 % and 15 % of that of the core component at 408 MHz (Lyne, 1971). The pulse profiles shows two distinct shapes: the more stable shape and a less stable one respectively referred to as *normal* and *abnormal* profiles or modes (see §2.7). At 610 MHz the ratio between the intensities of the leading and the trailing components is found to be randomly distributed with mean value of 0.56 and 1.17 for the normal and abnormal modes, respectively (Chen et al., 2011). This ratio increases with increasing frequency (Figure 2.4). Recently, Shang et al. (2017) analysed the pulse profiles taken from multi-frequency observations of the pulsar with a three-component model (see Figure 2.4a). It is noticed from their figure that the duty cycle of the pulsar at 610 MHz, for example, is about 10 % (approximately 30^o) and decreases with increasing observing frequency.

2.7 Mode Changes in PSR B0329+54

The mode changing characteristic of PSR B0329+54 was first reported by Lyne (1971). and was explained mainly as the relative changes in the brightness of the pulse components. In the normal mode, the ratio of the trailing to the leading components is more than unity while that of the abnormal mode is less than unity (Lyne, 1971; Chen et al., 2011).

The component on the rising side of the main component is more visible in the abnormal mode at 408 MHz.

Extending the study of mode switching in PSR B0329+54, Bartel et al. (1982) analysed this phenomenon over a wide range of frequencies, between 410 and 14.8 GHz (Figure 2.4b). The study showed a strong frequency dependence of the shape of the abnormal profile. The average intensity of the trailing component of the abnormal profiles increase with frequency. In particular, while the intensity of the trailing component was much lower than the main component of the abnormal mode at frequencies between 410 - 1400 MHz, the opposite was generally the case in the abnormal mode observed at frequencies between 2.7 - 14.8 GHz.

Another study by Suleĭmanova & Pugachev (2002) demonstrated that apart from the variation in the shape of the main component, its phase also varied during mode switching. In their 20-month observation interval at 111.39 MHz, they recorded four events in which PSR B0329+54 switched modes from normal to abnormal. They found during these events that the phase of the peak shifted by about 1-2 ms to the right during mode switch from the normal to the abnormal mode. In two of these events, the phase drift occurred gradually over several minutes as the mode switched. In the other two events, the shift was sudden, as usually assumed (e.g. Bartel et al., 1982). Similar phase shift behaviour in the leading component was also noticed, but was inconclusive for the trailing component at the selected observing frequencies due to a drastic reduction in intensity during the events. Also, it was found that the intensity variations in the outer components did not always correlate. These results led to the suggestion of a principal criterion for determining a mode switch in PSR B0329+54: the change of the intensity of the trailing component across a threshold of about 0.2 times its maximum average, as well as discrete shift of the phase of the main component.

It is generally agreed that there is an approximately 15 -20 % chances of detecting abnormal profiles in every observation, though up to 43 % chance is possible in shorter integrated profiles (e.g Lyne, 1971; Suleĭmanova & Pugachev, 2002; Chen et al., 2011). Additionally, the duration of each mode followed a gamma distribution and were independent of each other, with the pulsar typically spending 154 min and 32 min respectively in the normal and abnormal modes (Chen et al., 2011; Wang et al., 2012).

2.8 Timing Residuals of PSR B0329+54

The quasi-periodicity feature of the timing noise in PSR B0329+54 has led some authors to suggest the possibility of a companion planet. This suggestion was first made by Demiański & Prószyński (1979) based on the unexpected large value of the second derivative of the pulsar's rotational frequency ($\ddot{\nu}$) and a 3-year quasi-periodic feature present in the residuals. They argued that the best explanation to the large value of $\ddot{\nu}$ was the existence of a companion planet around the pulsar, choosing this ahead of other possibilities such as changes in pulse shape, precession of magnetic dipole axis or prior glitch events.

In the intervening years, as more observational data became available, the proposed orbital period of the companion planet was revised from 3-years (Demiański & Prószyński, 1979) to 16.9 years (Shabanova, 1995), and 27.8 years most recently (Starovoit & Rodin, 2017) even though the presence of the 3-year periodicity in the residuals was confirmed. Other authors disagreed with the ascription of the periodicity to the presence of a planetary body around the pulsar, instead concluding that the variations were the timing noise intrinsic to the pulsar (e.g Konacki et al., 1999; Hobbs et al., 2010b).

The timing residuals of PSR B0329+54 indicate the presence of two noise curves (see §3.2.3, Figure 3.4). These two noise curves have been ascribed to pulse profile changes

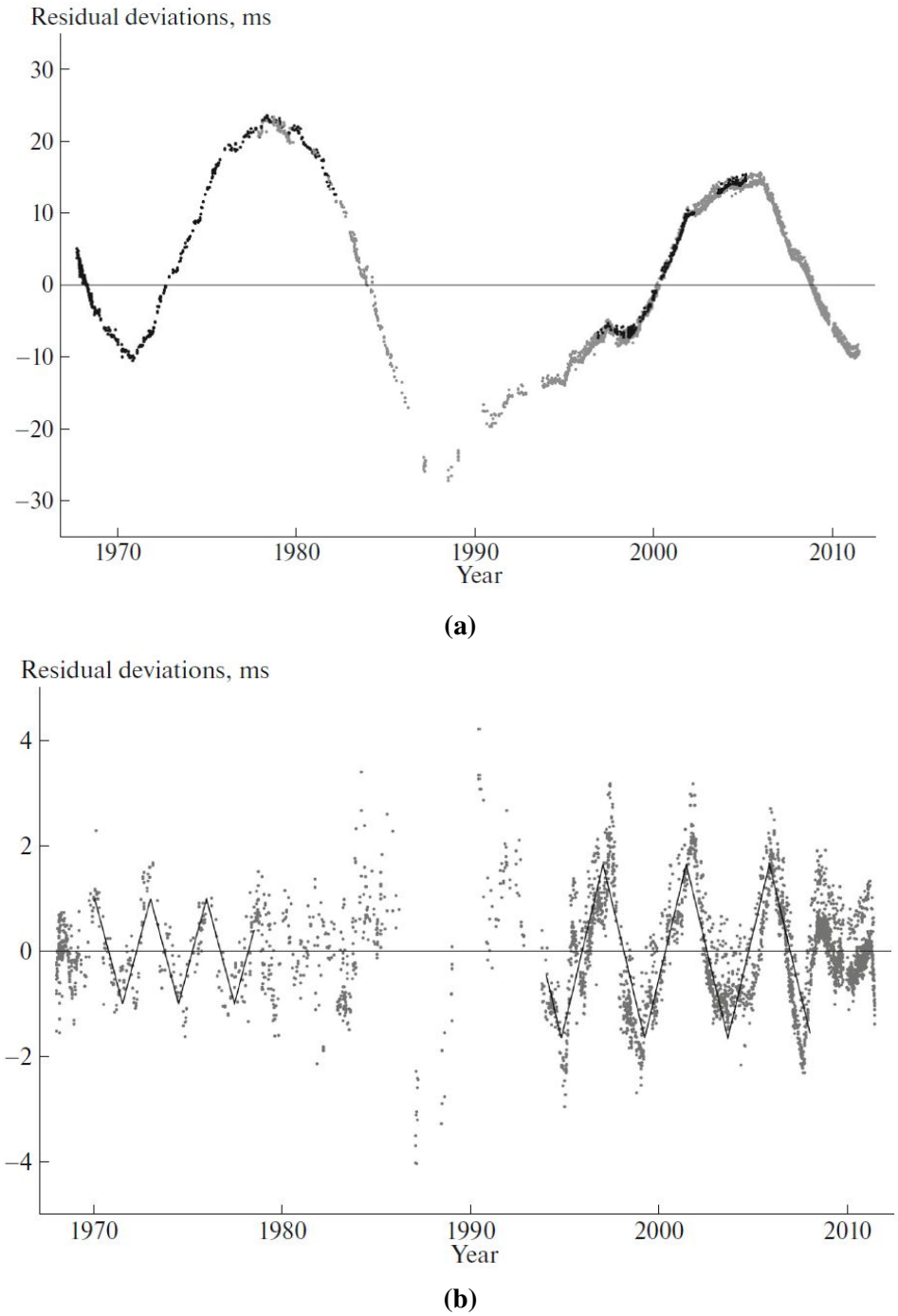

Figure 2.5: The timing residuals of PSR B0329+54 before (2.5a) and after (2.5b) the long term quasi-periodic structure was removed. Note the reappearance of the 3-year periodic structure (image taken from Starovoit & Rodin, 2017).

due to the pulsar's mode changing, leading to apparent variations in the TOAs derived from template matching (see §1.3) (Demiański & Prószyński, 1979; Starovoit & Rodin, 2017). In addition, two quasi-harmonic variations appear in the residuals: a shorter and more stable 3-year periodic modulation and a longer, less regular structure (Figure 2.5a). The former harmonic structure was found to have gradually disappeared in the timing residuals after 1979 (Konacki et al., 1999). The recent analysis by Starovoit & Rodin (2017) indicated that this 3-year harmonic behaviour in the timing residual resumed from about 1995 (Figure 2.5b).

Chapter 3

Observation and Data Processing

In this work, observation of PSR B0329+54 made with the 42-ft telescope at Jodrell Bank Observatory since late 2011 were used. The data were collected daily, with the so-called COBRA2 backend in the ultra high frequency (UHF) band of 610 MHz. The observation bandwidth was 5 MHz until the end of March 2012, and between 8 and 5 MHz was used thereafter until September, 2017.

The observations were performed with two polarizations, each divided into forty 250-kHz frequency channels in a filterbank, coherently de-dispersed and folded using DSPSR in real time (van Straten & Bailes, 2011). An integrated pulse profile (typically, the average of 84 contiguous pulses) is written out every minute with 1024 pulse phase bins. The observation lengths ranged between 30 - 40 min.

The data had already undergone pre-processing, such as the excision of frequency channels (mostly outer channels) that were badly affected by radio frequency interference (RFI). The phase bin values of all zapped sub-integrations are set to zero, and we referred to these as 'null' sub-integrations. Some observations were obtained during undergraduate practical sessions at Jodrell Bank. The data collected during practical sessions (every

Tuesday) could be recognised by the low S/N and the shorter observation length. The profiles of some observations were visually inspected together with their S/N to determine the criteria for selecting observation data for this work. An initial total of 1851 observations obtained was reduced to 1337, after removing (1) observations carried out during practical sessions and (2) observations with signal-to-noise ratio (S/N) of the integrated pulse profile below 30. The S/N of the integrated profiles ranged from 30 to 421, including 1064 (80 %) observations between 50 and 310. There were 25-day and 80-day observation gaps around mid-2014 and mid-2016, respectively, due to routine maintenance.

3.1 Data Reduction

Following the usual data storage format in pulsar astronomy, the Jodrell Bank Observatory stores observed pulsar data in PSRFITS, a standard Flexible Image Transport System (FITS) based storage format, fully integrated with PSRCHIVE for data analysis (Hotan et al., 2004).

The aim for reducing the data was to extract the "on-pulse window" covering the details of all the three of the brightest separate profile components. While this could be achieved by averaging a number of contiguous sub-integrations, resolving frequent mode switching time scales in PSR B0329+54 required rather shorter sub-integrations. At the same time it was important to maintain good signal-to-noise ratio to enhance classification accuracy. Hence 3-min sub-integrations were used, which was also consistent with previous research works on the mode changing of PSR B0329+54 (e.g. Lyne et al., 1971; Bartel et al., 1982; Chatterjee et al., 2000).

For every observation, the PSRCHIVE command "`pam`" was used to coherently scrunch all polarizations and frequency channels together. The outputs from this step had

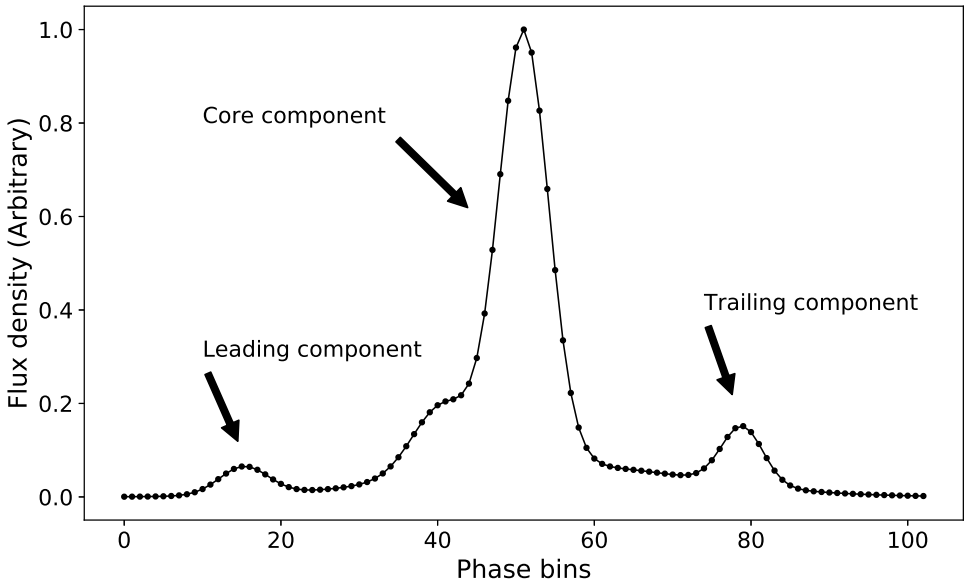

Figure 3.1: The profile of a reduced data sample showing the three brightest components. The integrated profile of an observation with high S/N has been used for clarity.

their sub-integration phases coherently scrunched in two ways and saved with different file extensions: (1) all sub-integrations were scrunched to obtain single pulse profile for each observation (hereafter referred to as .FTp files) and (2) three contiguous sub-integrations were scrunched together to obtain between 10 - 13 $\times$ 3-min sub-integrations for every observation (referred to as .3Fp hereafter).

Using another PSRCHIVE command, "`pdv`", the two sets of PSRFITS files (.FTp and .3Fp) were converted to ASCII format which is used to enable the application of python code. Also, it is assumed that the pulse profiles remained essentially the same for all observations, except for the instances of the mode changes. Hence, since the observational data were not calibrated, and given the large variance in the amplitudes of corresponding phase bins, the pulse amplitude values were normalised by the peak value within their respective sub-integrations. Moreover, it was determined that the main components of the

profile could be well presented with 103 pulse phase bins (i.e. 36^0 in spin latitude, 71 ms, or 10 % of the pulse period) with enough room to allow for pulse variations. The pulse windows were therefore extracted such that the main peak of the pulse profile fell on the 51st bin of the 103 phase bin wide pulse window (see Figure 3.1).

3.2 Machine Learning

Even though mode changing in PSR B0329+54 is associated with the corresponding variations in other observed emission properties such as polarization and full pulse width at half-maximum, variation in the intensity of the trailing component is most significant (e.g. Lyne, 1971; Taylor et al., 1975; Suleĭmanova & Pugachev, 2002). While many pulse profiles can be clearly identified with their mode class visually, for a significant number of the profiles it is difficult to clearly identify their mode classes. This difficulty arises due to the rapid rate of mode changing. Since each profile is made up of random fractions of either kind of pulse profile shape, there is no clear-cut threshold for identifying the profiles based on the intensity of the pulse components affected by the mode changing. Hence, for more than a thousand profiles, a robust technique was needed. Chen et al. (2011) applied a threshold in the relative intensity between the trailing and the leading component to classify the modes in PSR B0329+54. However, Tan (2014) used a machine learning technique to classify observations with excellent accuracy. Given the additional functionality of this technique in estimating performance metrics, machine learning was used in this project to identify modes of the pulsar, rather than visual inspection.

Machine learning refers to the application of computing power to learn and subsequently predict patterns in data without explicitly writing programs to do so (Samuel, 1959). In supervised machine learning classification, a sufficiently large human classified

data set is used to *train* or create a statistical model that represents the criteria for determining the class of a given instance of data. Training is followed by testing the model with another human classified instance of data from which a number of performance metrics could be evaluated to assess the performance. When the performance metrics are satisfactory enough the model can then be applied to classify large instances of similar data.

Various machine learning algorithms featured in the Scikit-learn library (Pedregosa et al., 2011) were exploited and assessed based on their performance metrics (classification accuracy, specificity and sensitivity). These included logistic regression (LR), k-nearest neighbour (KNN), linear discriminant analysis, Gaussian naive Bayes (NB), decision tree and support vector machines (SVMs).

The classifiers perform statistics on data using a set of i features, $\vec{a} = [a_1, a_2, ..., a_i]$, and decide to which one of the categorical populations or classes the sample belongs. In LR, the conditional probability of the sample belonging to one of the classes is assumed to follow a logistic function or distribution, ie. $P(1|a_1, a_2, ..., a_i) = \frac{1}{1-\exp^{-(\vec{a}^T\vec{w})}}$, where $\vec{w}$ is a weight vector chosen such that the log-likelihood is maximised during training. The KNN classification model locates each instance in an i-dimensional space using the features and each instance assumes the modal class of its k nearest neighbours. The distance between neighbours is usually the Euclidean distance given by $\sqrt{a_1^2 + a_2^2 + ... + a_i^2}$. The SVM similarly locates instances in k-dimensional space and learns the training set such that $\vec{w}^T\vec{a} + b > 0$, where $\vec{w}$ is the weight vector and the parameter $\frac{b}{||\vec{w}||}$, is the offset of the decision plane from the origin in the direction of $\vec{w}$.

The Gaussian NB classification model assumes the features or data values of each observation is normally distributed and estimates the parameters such as mean and standard deviation from the assumed distribution. The model is based on the Bayesian theorem

where the probability of a hypothetical parameter given the data values $P(h|a)$ is the product of the conditional probability of the data given the hypothetical value $P(a|h)$ and the probability of the hypothesis regardless of the data $P(h)$, ie. $P(h|a) = P(a|h)P(h)$. From the training set, the model calculates the posterior probabilities of each class by a simple ratio. It also evaluates the conditional probabilities of each class. For a new instance the probabilities of the parameters are used to estimate the posterior probability of each class. The new instance is then classified to be a member of the class with the greatest posterior probability. In the case of linear discrimination analysis, the conditional probability distribution functions (or the likelihoods) of the data for each class is assumed to be normally distributed with means of μ_1 for class 1 and μ_0 for class 0 but share a common covariance matrix Σ. Setting the logarithm of the ratio of the likelihood to a probability threshold leads to a linear boundary given by $2\vec{a}^T\Sigma^{-1}(\vec{\mu}_1 - \vec{\mu}_0) + \vec{\mu}_0^T\Sigma^{-1}\vec{\mu}_0 - \vec{\mu}_1^T\Sigma^{-1}\vec{\mu}_1 \geq T$ that is used to discriminate between the two class populations.

3.2.1 Training and Testing the Classification Models

In order to minimise over-fitting, only observations with integrated pulse profiles having S/N of 200 and above were used for training and testing the classification models. The integrated pulse profile of the observations were visually examined and assigned classes based on the intensity variations of the trailing component, as already described (§2.6 and 2.7). To avoid misclassifying "null" sub-integrations as either of the two classes or modes, fake instances of "null" profiles were included. These third mode data sets had zero intensity values for all their 103 phase bins, representing the zapped sub-integration. In total, 212 instances, of which 147 normal modes, 41 abnormal modes and 24 "null" modes, were used in training and testing the models.

In a 10-fold cross-validation process, the manually classified instances were reshuffled and split into 10 groups. 9 groups were used to train the model and the last group was used to test it. The percentage of correctly predicted instances is known as the classification accuracy. The 10-fold cross-validation process runs 10 times, each group used once as the test set. The average of the classification accuracies is then evaluated.

3.2.2 Classification Performance Metrics

In supervised machine learning classification, a good picture of the performance of the classifiers is obtained from the confusion matrix. The confusion matrix is a two dimensional array with the entries representing the frequencies of the outcomes of testing a classification algorithm. The rows represent the frequencies of the actual pre-assigned classes and the columns represent the frequencies of classes predicted on the training set by the algorithm used, consistent with how Scikit-learn displays the confusion matrix. An entry $M_{i,j}$, where $i, j \in \{\text{class 0, class 1, class 2, ... class n}\}$, in a confusion matrix M, is the number of instances with actual class i, that is predicted to be members of the class j. It follows that the leading diagonal of the confusion matrix (where $i = j$) represents the correct predictions, with false predictions everywhere else ($i \neq j$). In this work three classes were used; class 0 (abnormal mode), class 1 (normal mode) and class 9 ("null"). The classification metrics were calculated from the confusion matrix. They are defined as follows:

- *Classification accuracy* is the fraction of all instances whose classes were correctly predicted. From the confusion matrix, it is expressed as

$$Accuracy = \frac{\sum_{i=j}^{n} M_{i,j}}{\sum_{i=0,j=0}^{n} M_{i,j}}. \tag{3.1}$$

- *Sensitivity* is the fraction of all actual normal modes that were correctly predicted. Sensitivity can be calculated from the confusion matrix as

$$Sensitivity = \frac{M_{1,1}}{\sum_{j=0}^{n} M_{1,j}}. \tag{3.2}$$

- *Specificity* is the fraction of all actual abnormal mode instances that were correctly predicted and can be expressed as

$$Specificity = \frac{M_{0,0}}{\sum_{j=0}^{n} M_{0,j}}. \tag{3.3}$$

- *Precision* is the fraction of all predicted positive classes (normal modes) that were correct. In other words it is the probability of obtaining a correct prediction given that the predicted value is positive. The expression for precision is given as

$$Precision = \frac{M_{1,1}}{\sum_{i=0}^{n} M_{i,1}}. \tag{3.4}$$

Generally, the classification accuracies were remarkably high. In the 10-fold cross-validation process, Gaussian Naive Bayes and k-nearest neighbour scored the highest classification accuracy of 99.1 % and 99.0 % respectively, with the rest scoring between 71.4 % and 95.5 %.

From the above definitions, it is evident that maximum values of the performance metrics are preferable. Table 3.1 shows the classification performance of the algorithms based on the metrics. Even though all the classifiers had good classification accuracies ($\geq$ 85%), the shortfall in logistic regression and support vector machines indicates their inability to correctly predict any of the abnormal modes. K-nearest neighbour and Gaussian Naive Bayes were slightly less sensitive than the decision tree but were more specific

Algorithm	Accuracy	Sensitivity	Specificity	Precision
logistic regression (LR)	0.85	1.00	0.00	0.82
K-nearest neighbour (KNN)	0.99	0.99	1.00	1.00
Linear discriminant analysis (LDA)	0.92	0.92	0.88	0.97
Gaussian Naive Bayes (GNB)	0.99	0.99	1.00	1.00
Decision tree (DT)	0.99	1.00	0.94	0.99
Support vector machines (SVMs)	0.85	1.00	0.00	0.82

Table 3.1: Performance metrics of six classification algorithms. Generally, all the algorithms had good accuracy. However, LR and SVM were not specific, misclassifying all abnormal modes as normal but correctly predicting all normal mode (i.e. 100% sensitive). Even though LDA and DT were appreciably specific and precise, they were no match for KNN and GNB both of which were also nearly perfectly accurate and sensitive.

than the decision tree and linear discriminant analysis classification algorithms.

In each of the confusion matrices, all "null" modes were correctly classified and none of the normal or the abnormal modes were incorrectly classified as "null". Hence, it was assumed that the classifiers reliably distinguished the "nulls" from the other modes. Also note that the classification performance results presented in table 3.1 are based on a single train-test procedure, in which the manually classified profiles are split into two groups, one for the training and the other for testing. Hence the marginal difference between the 5-fold classification accuracies of Gaussian naive Bayes and k-nearest neighbour classifiers indicated that the former was more reliable. Gaussian naive Bayes was therefore used to classify the integrated pulse profiles (.FTp in ASCII format) and the 3-min sub-integrated profiles (.3Fp in ASCII format) within every observation.

3.2.3 Validating the Classification Performance

Further statistical analysis of the known properties that differentiate the two modes were performed to validate the performance of the classifier. The first was the mean height of the trailing component of each observation (see Figure 3.2). Mindful of the phase offset of the peaks of the trailing components between the two modes, the mean height was obtained by averaging the 75th through the 81st phase bin values of the reduced data. The histograms of the distributions are shown in Figure 3.3a. Using a Kolmogorov-Smirnov (K-S) test it was confirmed that the height of the normal modes followed a normal distribution at 95% confidence level. The best fitted normal distribution has a mean of 0.13 and standard deviation of 0.01. These show that the trailing component of the normal mode has more stable intensity than that of the leading component, consistent with earlier studies (e.g. Helfand et al., 1975; Chen et al., 2011). However, the histogram of the abnormal mode is broader and shows bimodal distribution. This indicate that the set of observations classified as abnormal mode, might consist of two modes. As seen in Figure 3.3a, its trailing tail, which also bears the minor modes of the histogram, overlaps with the leading tail of the histogram for the normal mode. There is an even greater overlap in the histogram of the mean height of the leading component (Figure 3.3c). Hence if the high classification accuracy extends to observations with S/N as low as 30, then these results suggest that the mode of a pulse profile was not determined by the height of the leading and trailing components only but a combination, which demonstrates the value of the machine learning.

Following the pulse shape difference between the two modes, visible from inspection of the profile, the distribution of the average full width at 50% of maximum (FWHM or w_{50}) for each mode was also considered (Figure 3.3c). The distributions of FWHM for

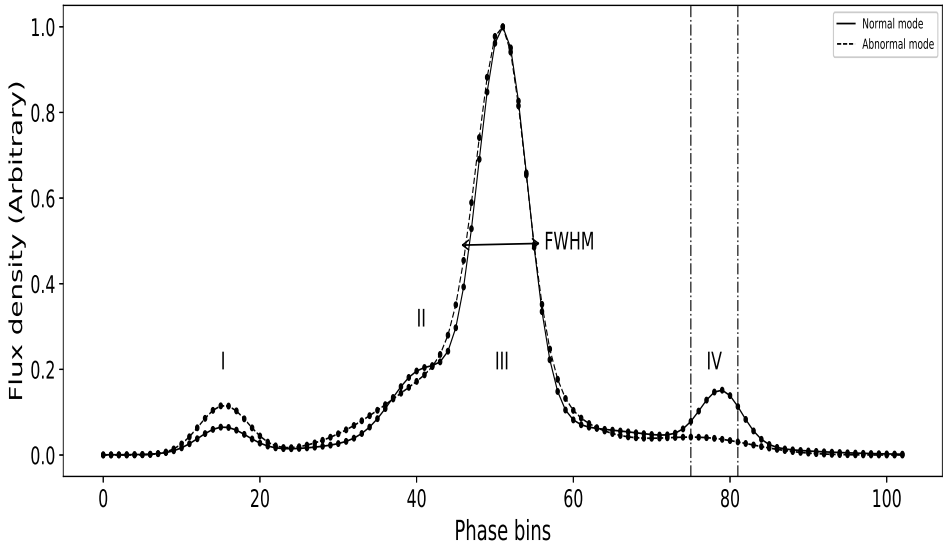

Figure 3.2: Typical shapes of the two profile modes at 610 MHz showing the leading (I), the core (III) and the trailing (IV) components. The shape of the "saddle" component (II) on the rising side of the core component show significant difference between the two profiles and the abnormal mode profile shows a wider FWHM. Also, there is an apparent phase offset of the peaks of the trailing components between the two profiles (apparently within the phase bins indicated with the dashed vertical lines).

both modes can be well described as Gaussian. As expected, the mean w_{50} value for the abnormal mode was slightly greater than that of the normal mode. At 68% confidence level, the mean FWHM are $\mu_{abnormal}$ = 8.32$\pm$0.19 and μ_{normal} = 7.93$\pm$0.20.

A two-sample K-S test was used to compare the statistical significance of the two distributions of each parameter. At a 5% significance level, the absolute difference between the respective empirical cumulative distribution functions were greater than the critical value, leading to the rejection of the null hypothesis that the two distributions were similar. Hence the conclusion that the classified modes were of different populations and that the classification performance was acceptable.

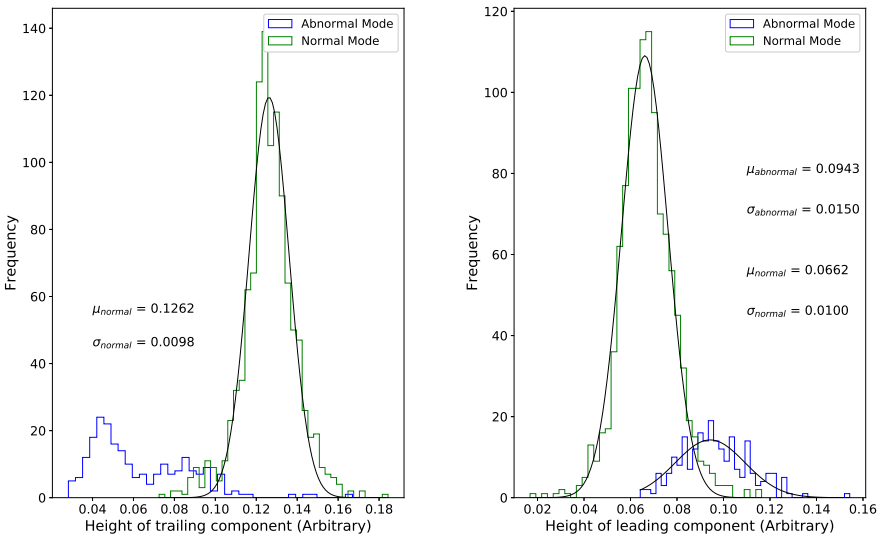

(a) **(b)**

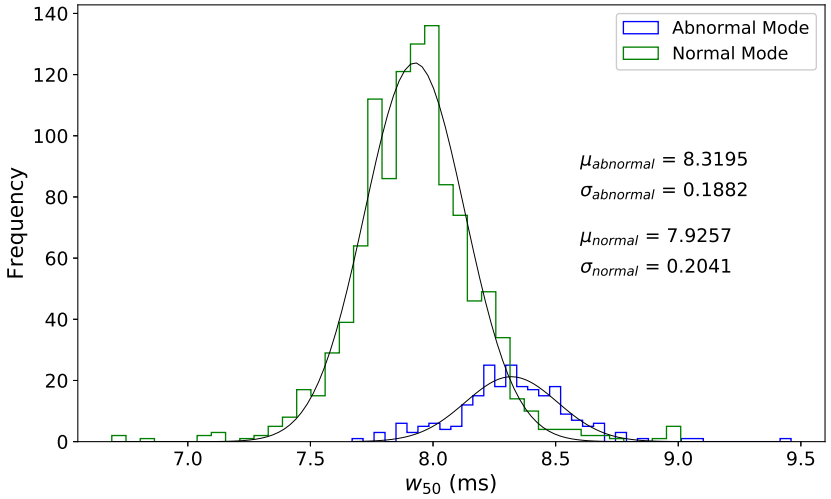

(c)

Figure 3.3: The histogram of (a) the mean heights of the trailing components, (b) the mean heights of the leading components and (c) the average full width at half maximum (FWHM) of the classified integrated profiles. The histogram of the normal mode in (a) follows a normal distribution with mean μ = 0.13±0.01 (at 68% confidence level) while that of the abnormal mode shows a multimodal distribution. Both histograms in (c) follow normal distributions fairly well. The mean FWHM values are $\mu_{abnormal}$ = 8.32±0.19 and μ_{normal} = 7.93±0.20 (at 68% confidence level). A two-sample K-S test performed using the height of the trailing components and the FWHM showed that the distributions of the modes were different in both cases, confirming the distinction between the two modes.

3.2.4 Classified Modes and the Timing Residuals

Using our Jodrell Bank observations, the TOAs for the two modes were created. A single template was used and timing was performed at once for all the TOAs with the same ephemeris (see § 1.3.3 for details). The plot of the timing residuals for the two modes is shown in Figure 3.4. Each residual point was matched to the mode class assigned to its corresponding integrated pulse profile using Gaussian Naive Bayes classifications. Figure 3.4 shows that the residuals of the abnormal modes have an offset, as they are almost always located above the immediately normal mode residuals. This would be expected if the deviations from the normal curve were exclusively due to the cross-correlation between the template and the profiles. This is because the average profiles of the abnormal modes have a higher flux in the leading component and in the leading edge of the main component than that of the normal mode. Also, the residuals for the normal modes have smaller scatter than that of the abnormal modes. This suggests that the normal mode profiles have more stable shapes. The separation of the residuals corresponds directly with the mode identified, showing that the machine learning classification was successful.

3.3 Estimating Fractional Occurrence of Normal Mode

The ASCII format of each .3Fp file (see § 3.1) contained all the 3-min sub-integration instances of the given observation. This allowed the fractional occurrence of the normal mode to be estimated for each observation. These 3-min sub-integration instances of a given observation were classified independently and the proportion of the normal modes out of the total number of classified normal and abnormal modes were estimated.

Mindful of the low S/N of the 3-min sub-integration relative to the integrated profiles, which could degrade the classification performance, the fractional occurrence of the

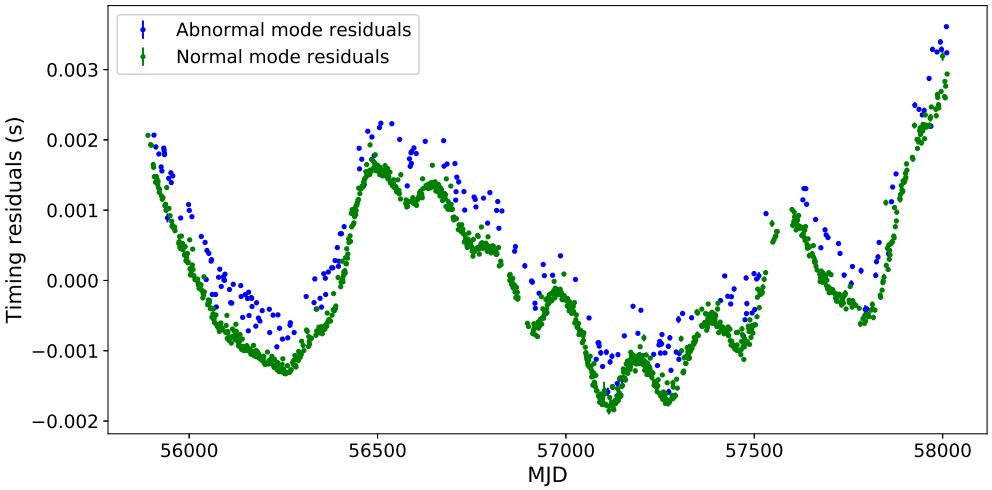

Figure 3.4: Timing residuals of classified observations. Even though the residuals of the two modes track each other, that of the abnormal modes are offset and scatter in a broader track. This apparent displacement of the abnormal mode residuals agrees with prior knowledge of the residual plots before the machine learning technique was applied.

normal mode was compared with the corresponding mode of the integrated pulse profile for the given observation in order to validate the classification of the former. The distributions of the fractional occurrence are shown for the normal mode and the abnormal mode in Figure 3.5. As would be expected, the histograms show that the mode of the integrated pulse profile can be predicted given the fractional occurrence of the observation with fairly good accuracy. The fractional occurrence of the abnormal mode profiles generally fall below 0.5 while that of the normal mode profiles is generally above 0.5. In particular, the fractional occurrence cut-off points were 0.67 and 0.23 for the abnormal and the normal classes respectively (Figures 3.5 a and 3.5 c).

The graph of fractional occurrence against the date of observation (in MJD) was smoothed using the sliding average smoothing technique. First, contiguous observations within a 15-day window (kernel) were averaged together with 5-day strides. This was

repeated for a 30-day window with 10-day strides and a 60-day window with 20-day strides. The results were compared as shown in Figure 3.6. We find that all the three smooth curves track each other fairly and can represent the moving average of the fractional occurrence.

The fractional occurrence curve has a quasi-periodic modulation of about 185-days between MJD 56400 and 57500. The modulation has wider local maxima and narrower local minima. This indicates that a secondary quasi-periodic mechanism could be at work that is fairly closely associated with mode changing of the pulsar. It also suggests that the time-scale of mode changing, is itself, varying with time. Specifically, the pulsar is switching between two states: a relatively long-term state in which the pulsar spends more time in the normal mode and a short-term state in which the pulsar spends more time in the abnormal mode. Moreover, the running average of the fractional occurrence seems to follow a long-term parabolic function indicating a gradual shift in mode stability from the normal mode to the abnormal mode. However, no apparent reason could be assigned to this trend.

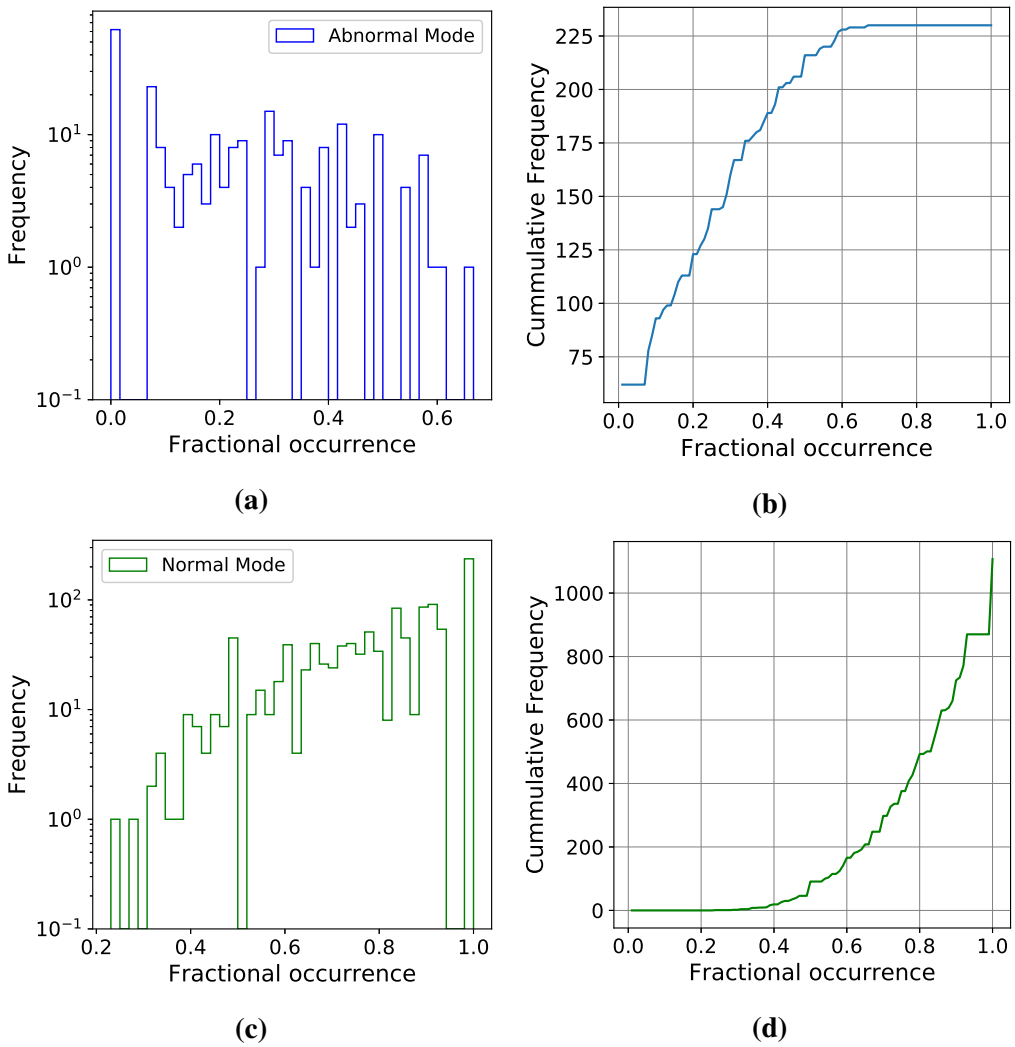

Figure 3.5: The histogram and the cumulative frequency distributions of the fractional occurrence for the abnormal mode (upper panel) and the normal mode (lower panel). The histograms are shown with the frequency counts on a log-scale to bring out the details. Taking a fractional occurrence threshold of 0.5, the cumulative frequency curves show that approximately 85% of the classes of the 3-min sub-integrations matched their corresponding classes of the integrated pulse profiles.

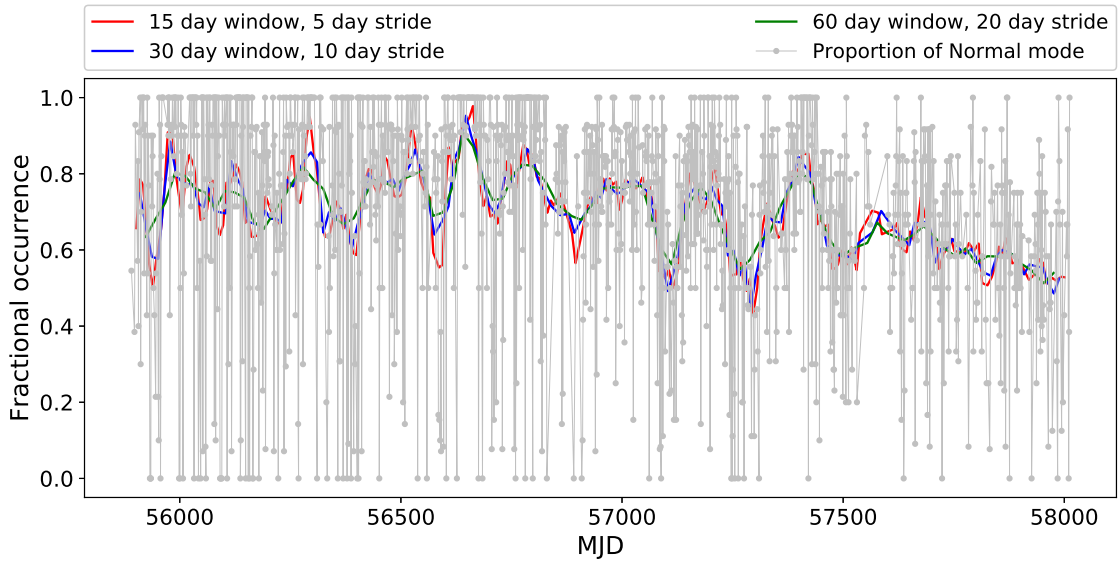

Figure 3.6: A plot of fractional occurrence and its smoothed curve overlaid. The smooth curves track each other with a quasi-periodic modulation of about 185 days, indicating a secondary magnetospheric effect associated with mode changing. Also, the average fractional occurrence gradually reduces towards 0.5.

Chapter 4

The Apparent Relationship Between Pulse Shape and Spin-down Rate

Determining the TOAs of pulse profiles is based on the assumption that each observed pulse profile is a shifted, weighted and noisy version of a definite template which does not vary during the entire time scale of the observations (Taylor, 1992). With this assumption, a characteristic fiducial point is defined as the phase bin of the peak value of the template. For a perfect pulsar, the timing residuals should have a normal distribution with a width corresponding to the individual TOA errors. However, the shapes of the pulses vary from one to the other due to uncorrelated noise, variations in spin rate and emission irregularities of the pulsar. Typically when a sufficiently large number of pulses (usually approximately a thousand pulses are required) are averaged together, the shape of the resultant integrated pulse profile is stable. However, the pulse profiles are not always scaled and shifted versions of the template, in practice. These variations can translate into some of the deviations of the TOAs from the timing model. These variations may be further affected by the choice of the template used to create the TOAs. Apparently,

in PSR B0329+54 the residuals of the abnormal mode TOAs are offset from those of the normal mode by a range of values.

As demonstrated by Lyne et al. (2010), the spin down rate can vary with changes in the pulse shape, contributing to the timing noise. In this chapter, the relative effect of the choice of a template has on the value of the TOAs are assessed. The link between the fractional occurrence of the normal mode and the amplitude of the timing noise of PSR B0329+54, will also be considered.

4.1 The Effect of Template Selection

4.1.1 Generating Templates

Since timing residuals depend, to some extent, on the shape of the template used, two reference templates were created from "pure" profiles, one for each mode class in order to analyse this effect. The selected profiles were "pure" in the sense that all the 3-min sub-integrations and the integrated profiles used to form a given template had the same mode class. This was to ensure that the time scale of the mode changes is resolved as best as the 3-min sub-integrations allow. The observed profiles with the highest S/N were chosen for creating the template. Among the observations with the normal mode profiles, the highest S/N is 421 and the highest S/N among the abnormal mode is 339. Most observations had thirteen 3-min sub-integrations; depending on the observation length, some were in excess of 1-min or 2-min sub-integrations. All 3-min and the excess sub-integrations, if any, were classified. Using the PSRCHIVE command `paas`, two reference templates were obtained by fitting sums of von Mises functions to the selected pulse profiles as described in §1.3.2. The command also allows the values of every component to be saved in text

files, which were subsequently used to plot the template shown in Figure 4.1.

4.1.2 The Shape of the Template and TOA Uncertainty

To expand the test for the dependence of the timing residuals on the shape of the template, 27 more test templates were created from selected profiles with S/Ns $\geq$200 and with varied fractional occurrence of the normal modes. The idea was to investigate the link between the fractional occurrences (representing the shapes of the templates) and the time shift due to cross-correlation. It was expected that the effect of shape variations would reflect in the time lag. It was also to obtain the range of time shifts that can be introduced by the templates (the "pure" normal template was used) by cross-correlation.

Since cross-correlation measures the time shift between two templates at which there is maximum overlap of the area under the curves, it is expected that the distribution of time shift would reflect the variation of the template shapes and the subsequent effect on the timing residuals, due to the template selection. The command used to create TOAs implements the cross-correlation by Fourier transforming the data series according to the cross-correlation theorem: $f \otimes g = F^* \cdot G$, where F and G are the Fourier transforms of discrete time functions, f and g respectively and "*" indicates the complex conjugate. This allowed time lags in fractions of phase bin intervals to be calculated. In this work, a script written in python was used to implement the cross-correlation represented mathematically as $f \otimes g = \sum f[t]\, g[t+\tau]$. Anticipating that the precision of the phase lags could be smaller than the phase bin resolution, the 27 test templates (as well as copies of the reference templates) were reproduced with 10,000 bins (see Figure 4.2). Also, all reproduced templates were centred on the maximum peak before the cross-correlation so that the time lag is primarily due to the shape rather than the positions of the templates.

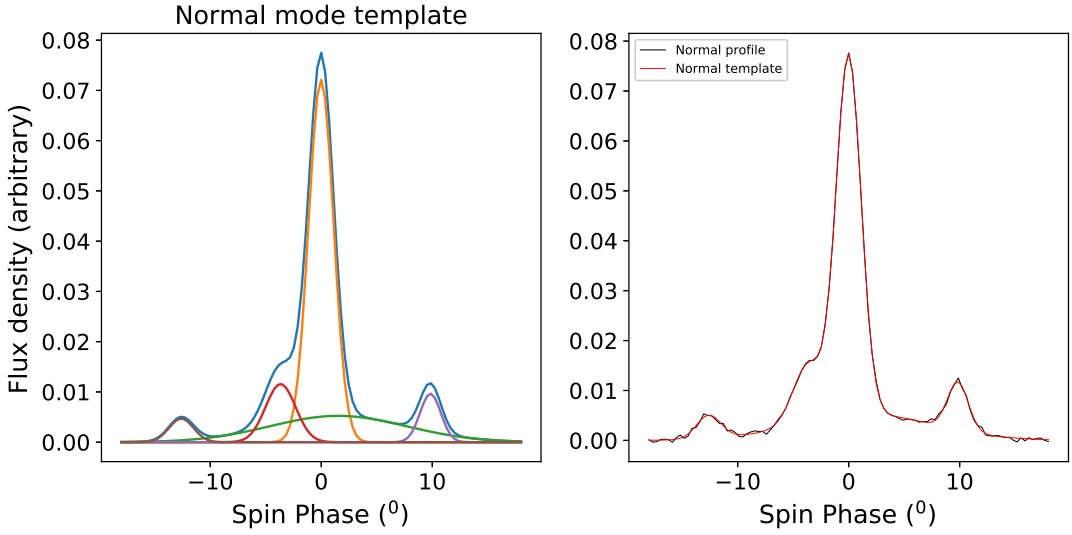

(a)

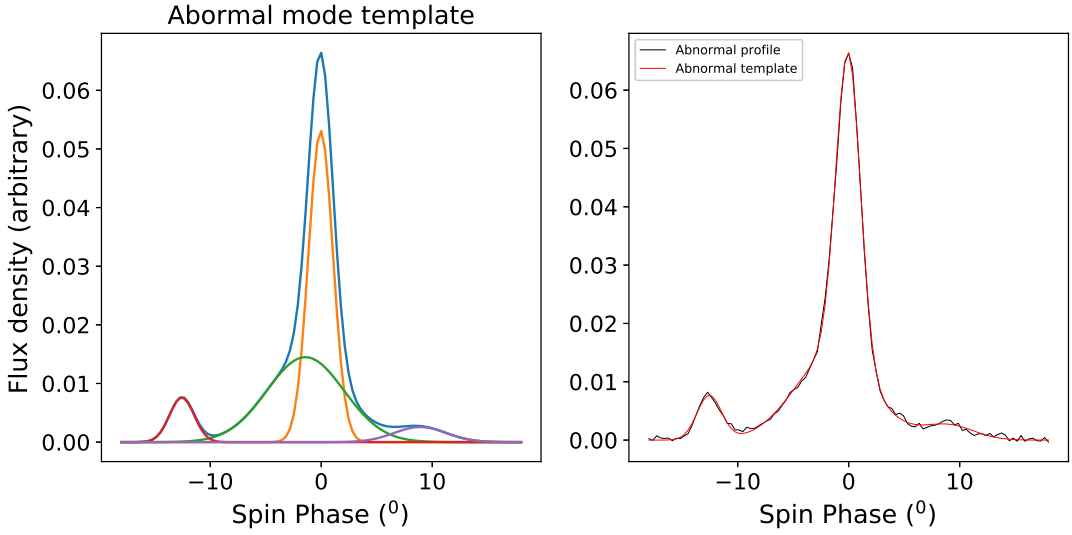

(b)

Figure 4.1: Templates of (a) a normal mode profile and (b) an abnormal mode profile. The observations from which they were created had S/N of 421 and 338 respectively. The von Mises components are shown together with the resultant profiles (in blue on the left). The noisy data profiles (black) are overlaid with the respective mode template (red) on the right to demonstrate how best the templates represent the data. The figures are zoomed in to the narrow phase range.

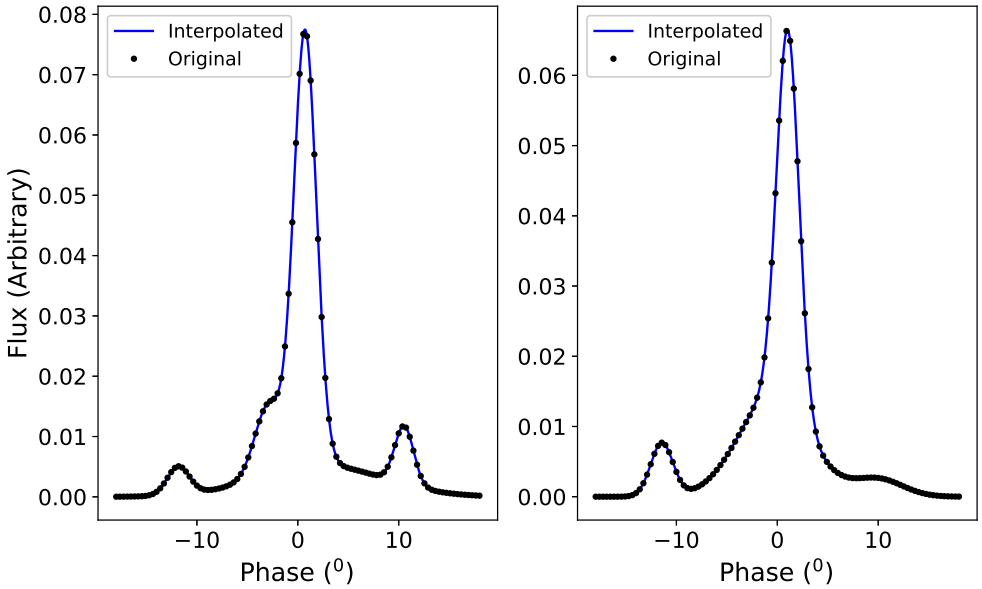

Figure 4.2: Sample interpolated template with 10,000 bins; normal mode is on the left and abnormal mode is on the right. The phase bin of the fiducial point of the interpolated template may not be the same as that of the original template.

Figure 4.3 shows the scatter plot of the time lags as a function of the fractional occurrence of the normal mode as well as the histogram of the distribution of the time lags.

As shown in Figure 4.3, there is greater preference for a phase lag of 0.02^0 (or 39.67 μs). Also, the lag range of 0.1^0 suggested that the choice of the template introduced a maximum delay of approximately 198 μs in the TOA. This is about 10 times greater than the typical TOA error of 25 μs, indicating a significant effect on the TOA depending on the shape of the template used. However, the plot does not confirm correlation between the phase lag and the fractional occurrence of the normal mode in observations. This may be due to the small sample used compared to the total number of observations.

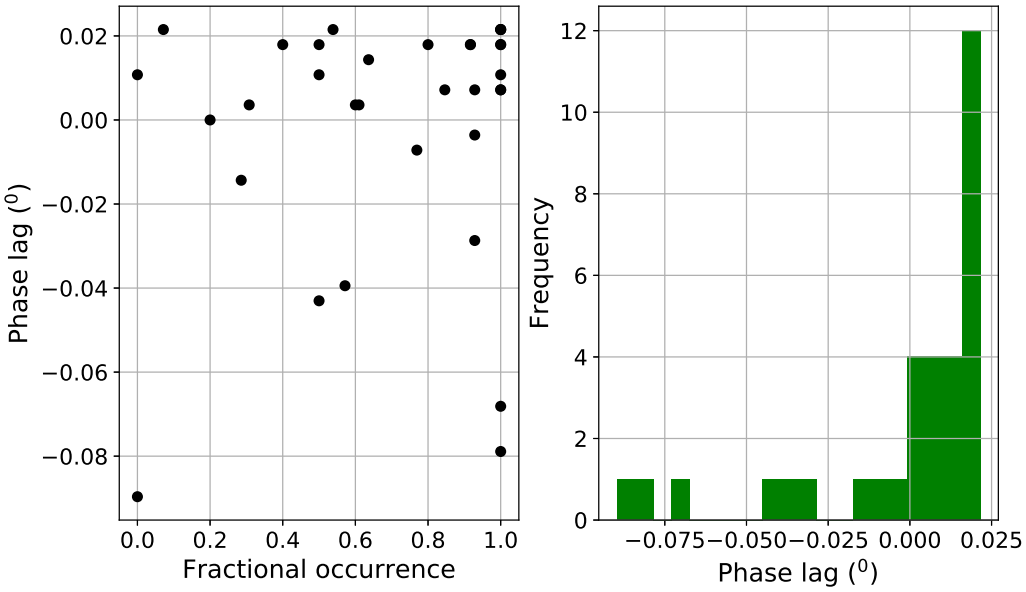

Figure 4.3: A scatter plot (left) and a histogram (right) showing the likely range of phase lag that may be associated with generating TOAs.

4.2 The Effect of Mode Profile and Template Selection

To investigate the effects of the mode profiles and the reference templates together, four sets of TOAs were generated by the template matching method described in §1.3.2. The PSRCHIVE command "`pat` was used to generate four sets of TOAs:

- normal mode profiles with normal mode template (NPNT)
- abnormal mode profiles with normal mode template (APNT)
- normal mode profiles with abnormal mode template (NPAT) and
- abnormal mode profiles with abnormal mode template (APAT)

For each set of TOAs, the TEMPO2 software package was used to fit a timing model to the TOAs. The list of parameters fitted is provided in Table 4.1. Note that only integrated pulse profiles were used in creating the TOAs. The same Solar System ephemeris

Parameters	Value
Time span of observations (yrs)	5.8
Number of TOAs	1337
Error-weighted residual RMS (μs)	977.129
Reduced χ^2 value	2.26
Right ascension (h : m : s)	03:32:59.407 (2)
Declination (^{0}: ’ : ")	+54:34:43.40 (3)
Spin frequency (s^{-1})	1.399538215441 (3)
Frequency derivative (s^{-2})	-4.00255 (3)$\times 10^{-15}$
Dispersion Measure (pc cm^{-3})	26 (4)
Reference epoch (MJD)	56950
Observation frequency (MHZ)	610
Start (MJD)	55889
Finish (MJD)	58013
Solar System Ephemeris	DE421

Table 4.1: Post-fit timing solution using TOAs from all profiles from both sets of modes.

(DE421) was used in performing all pulsar timing, for consistency. For every two sets of residuals, an average time offset is evaluated. The time offset presumed to take account of the systematic delays arising from either using templates of different shapes/modes or profiles of different shapes/modes. Comparing the offset value would provide additional insight into its dependence on the choice of template or otherwise, on the mode of the pulse profile.

For the sets of residuals of the same mode profile, the root mean square error (RMSE) is used as the average time offset between the two sets. The RMSE $=\sqrt{\frac{\Sigma(R_{1,i}-R_{2,i})^2}{N_{TOA}}}$, where $R_{1,i}$ and $R_{2,i}$ are the ith residual values of the given two sets and N_{TOA} is the number of TOAs of one set. For the sets of residuals of different mode profiles, the *JUMP* command in the TEMPO2 software package was used to fit a constant phase offset between data sets.

4.2.1 TOAs of the Normal Mode Profiles (NPNT and NPAT)

The residuals of the two sets of TOAs of only the normal mode profiles (i.e. NPNT and NPAT) are compared. A plot of the full data set and a short section of the residuals are plotted in Figure 4.4. The residuals of NPNT are indicated with black and that of NPAT are indicated with red.

These plots do clearly show significant time offsets between the two sets of residuals. The time offset shown in Figure 4.4 is 137.9 μs. Also, the average of the uncertainties for NPNT set is 22.5 μs and that of the NPAP set is 27.6 μs. This shows that the RMSE of the time offset is larger than the average of the uncertainties by a factor of approximately 5, indicating that this statistically significant time offset is due to the choice of the template.

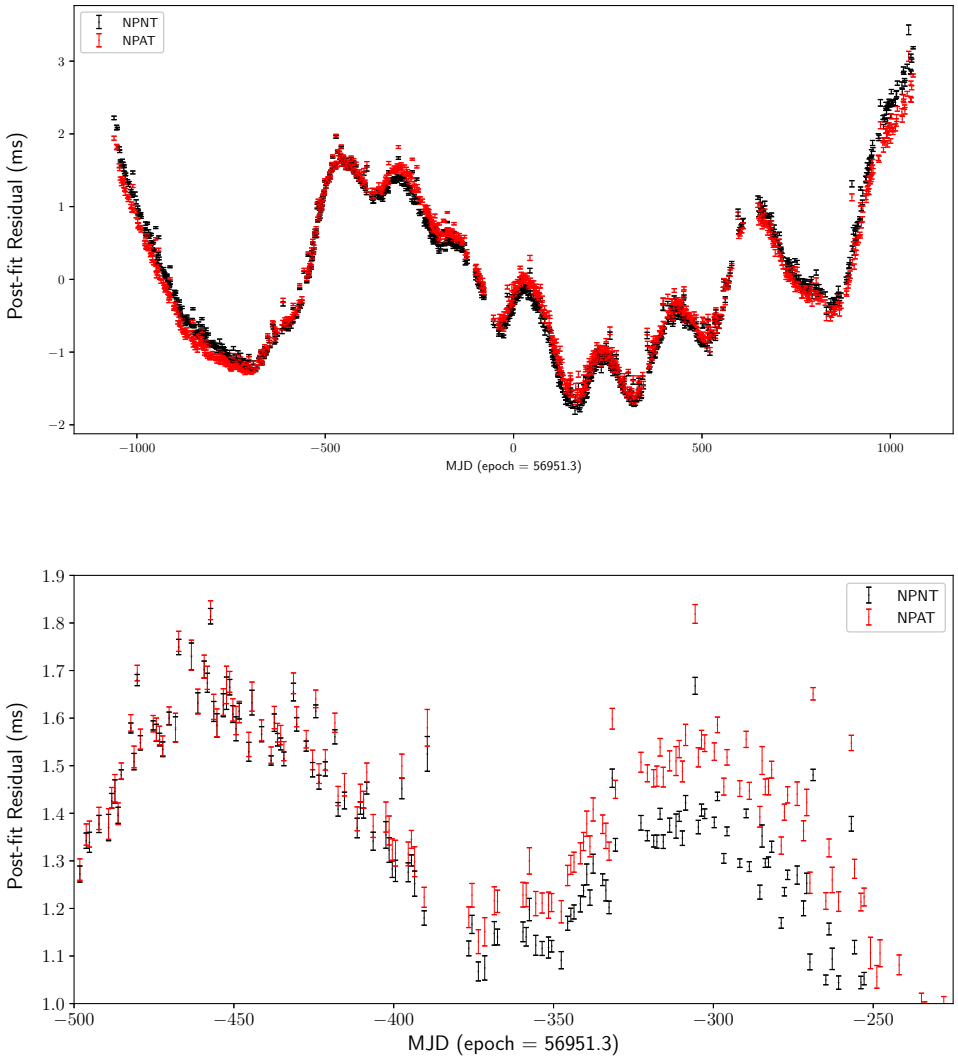

Figure 4.4: The post-fit timing residuals of TOAs of normal mode profiles only: the residuals obtained with the normal template, i.e. NPNT (black) and the ones obtained with abnormal template, i.e. NPAT (red). The upper panel shows the full data set and the lower panel shows a short section to make the time offsets more visible. The root mean square error is 138 μs.

4.2.2 TOAs of the Abnormal Mode Profiles (APNT and APAT)

Figure 4.5 shows the two sets of residuals of TOAs of the abnormal mode profiles; the set obtained using the normal mode template (i.e. APNT, in green) and the set obtained by using the abnormal mode template (i.e. APAT, in blue).

Again, the RMSE of their time offsets is 81.7 μs. This is approximately 3 to 4 times greater than the average value of the residuals uncertainties (26.9 μs for APNT and 23.5 μs for APAT) which seem to suggest statistically significant difference between the two sets of residuals. This indicates that the difference is solely due to the choice of the templates. In addition, it is noted that the template mismatch, as in the case of APNT, results in larger TOA uncertainties, as is expected.

4.2.3 TOAs of the Normal Mode Template (NPNT and APNT)

Now the post-fit residuals of the TOAs of both mode profiles created with the normal mode templates (NPNT and APNT) are analysed and compared with the findings in the last two subsections. The residuals of the two sets are plotted in Figure 4.6.

It can be seen that the time offset between the two curves are significant compared to that seen in Figure 4.4 and Figure 4.5. A *JUMP* command option of the TEMPO2 software package, was used to measure the average systematic offset between the two curves. This was measured to be 424 μs. Recall that the average time offset of 138 μs recorded in Figure 4.4 (see § 4.2.1) was the highest arising from using two sets of residuals obtained with templates of different modes. This 424 μs is significant and it is about 3 times greater than 138 μs offset. This result suggests that the time offset between the normal mode residual curve and the abnormal mode residual curve may not be the effect of using the normal mode template.

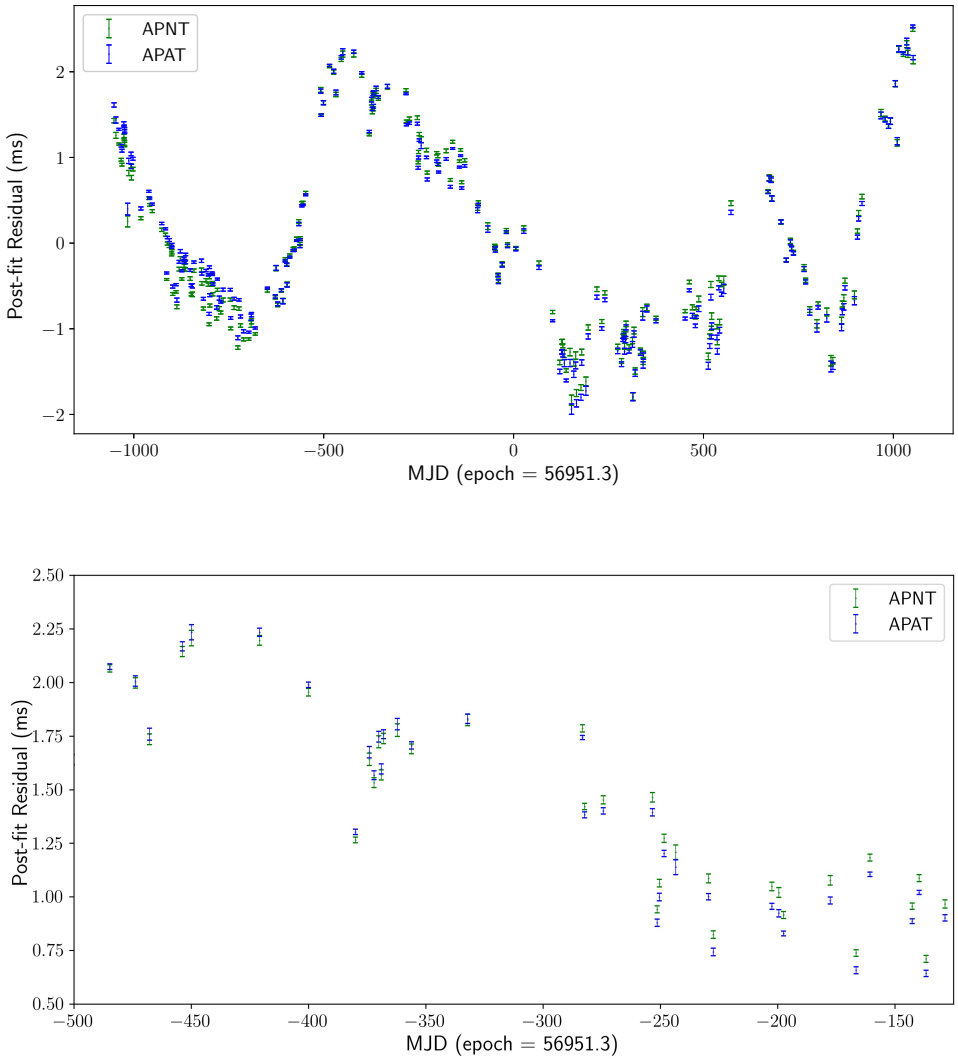

Figure 4.5: The post-fit timing residuals of TOAs of abnormal mode profiles: the residuals obtained with the normal template (green) and the ones obtained with abnormal template (blue). The upper panel shows the full plot and the lower panel shows a section to make the time offsets more visible. The root mean square error is 82 μs.

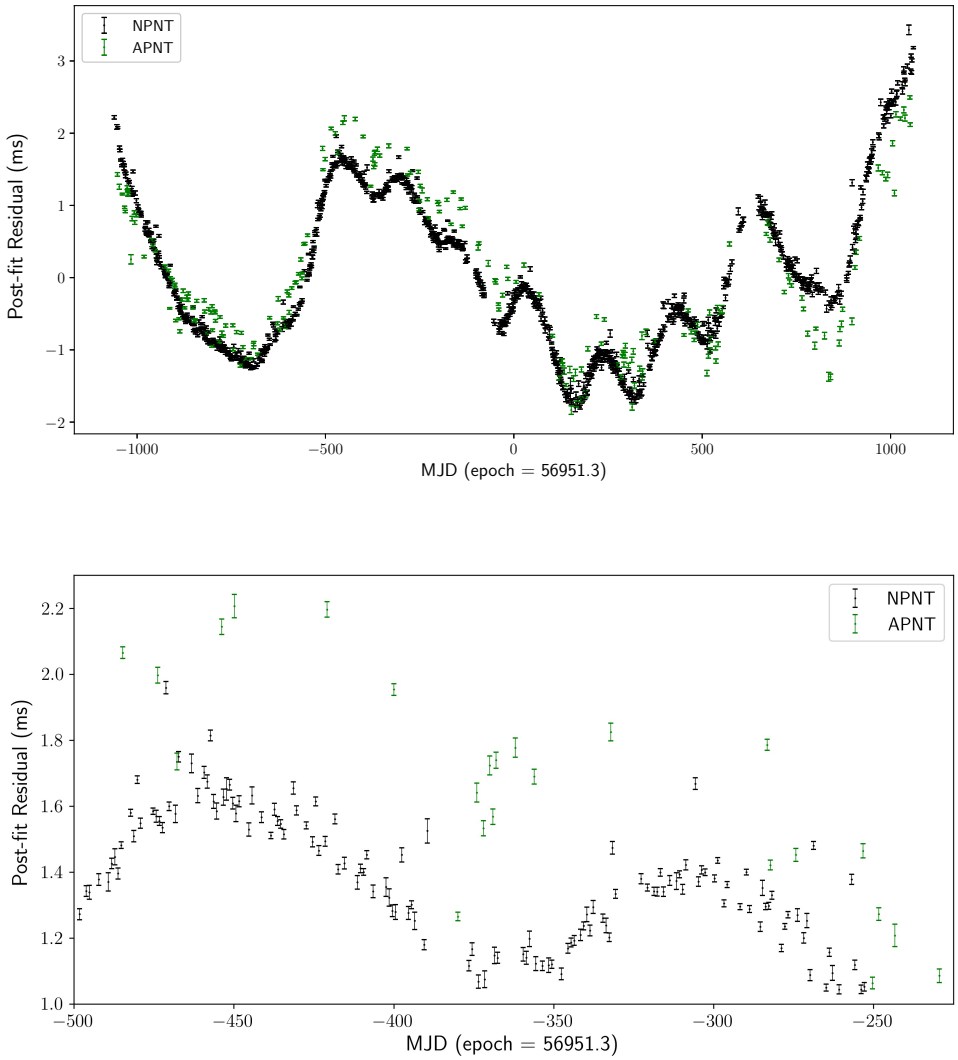

Figure 4.6: The post-fit timing residuals of TOAs of all observations (black for NPNT and green for APNT). The upper panel shows the full plot and the lower panel shows a section of the plot for clearer view of the time offsets. The average time offset between the two curves is 424 μs.

Profile Mode	Template Mode	RMSE	JUMP	Refer to
Normal	Normal Abnormal	138 μs	-	Figure 4.4
Abnormal	Normal Abnormal	82 μs	-	Figure 4.5
Normal Abnormal	Normal	-	424 μs	Figure 4.6
Normal Abnormal	Abnormal	-	460 μs	Figure 4.7

Table 4.2: Summary of the analysis of the average time offsets. Each row identifies the set of TOAs; the mode of the pulse profiles as well as the mode of the template used to create the set TOAs. The average time offsets between the sets of residuals are given under the RMSE or the JUMP heading. The appropriate figure is indicated for quick reference in the last column.

4.2.4 TOAs of the Abnormal Mode Template (NPAT and APAT)

The plot for the residuals of all TOAs obtained by matching both mode profiles to an abnormal mode template (i.e. NPAT and APAT) is shown in Figure 4.7. The average time offset between the two residual curves is measured with the *JUMP* feature of the TEMPO2 package and it was found to be 460 μs. Again, this is about 3 times greater than what would be expected if this time offset was due to the use of the abnormal mode template.

4.2.5 Summary of the Relative Effect of the Shape of Pulse profile and Template

The mathematical principle behind the creation of TOAs by matching a template of high S/N explains why variations in the shape of the template changes the magnitude of the residuals. However, there are compelling reasons that the variations of both the pulse shape and times of pulse arrivals may arise from the changes in physical conditions in the

pulsar magnetosphere (Lyne et al., 2010). In the analysis of the effect of the template, it was revealed that the two mode templates contributes to the uncertainties of TOAs of the normal mode profiles (NPNT and NPAT) by approximately 138 μs and that of the abnormal mode profiles (APNT and APAT) by 82 μs (see the summary of the results in Table 4.2). This is quite consistent with the range of time offsets (i.e. 198 μs which was described in § 4.1.2).

However, the residuals of both mode profiles obtained with the normal template (i.e. NPNT and APNT) shows an average time offset of 424 μs. Also, the residuals of both mode profiles obtained with the abnormal mode template (i.e. NPAT and APAT) show an average time offset of 460 μs. These time offsets (i.e. 424 μs and 460 μs) are approximately 3 to 5 times what would be expected if the time offsets were caused by the choice of template. Hence it may be more convenient to attribute the time offset to the variation in the rotation torque due to magnetospheric changes (Lyne et al., 2010). Another possibility is that the site of emission changes with mode changes (Lyne & Graham-Smith, 2005).

4.3 The Effect of Fitting Timing Parameters

Statistically, the goodness of fit is strongly dependent on the number of instances or data points. Since the number of the normal mode residuals differs very much from that of the abnormal mode residuals (in ratio of approximately 1:5), it is possible that the time offsets have been affected by the timing model. The effect was assessed by comparing the weighted RMS of the timing solution for each set of TOAs. The reduced χ^2 or (χ^2_r) values were also compared. The weighted RMS is one measure of the level of timing noise (see §1.3.6) and the χ^2_r expresses the goodness of fit (see § 1.3.3). These two parameters were

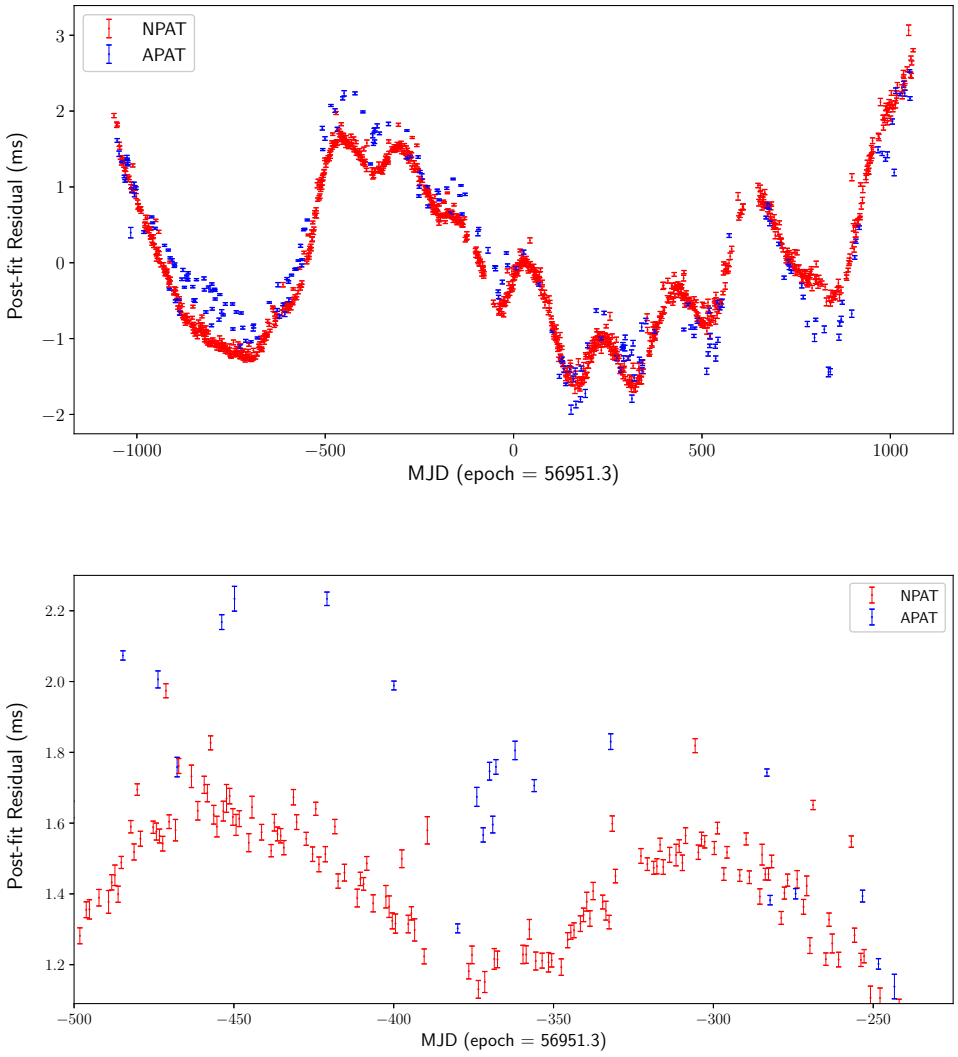

Figure 4.7: The post-fit timing residuals of TOAs of all observations (red for normal mode and blue for abnormal mode) created with the abnormal template. The upper panel shows the full plot and the lower panel shows a section of the plot for clearer view of the time offsets. The average time offset between the two curves is $460\,\mu$s.

Profile Mode	Template Mode	RMS (μs)	χ^2_r (DoF)
All	Normal	977.13	2.26 (1332)
Normal	Normal	968.26	2.69 (1102)
Normal	Abnormal	976.57	2.23 (1102)
Abnormal	Normal	961.57	8.79 (225)
Abnormal	Abnormal	932.7520	10.54 (225)

Table 4.3: Some selected post-fit timing results for comparison. Each set of TOA was independently timed.

chosen for convenience.

As the full plots in Figures 4.4 through 4.7 show, each set of the timing residuals essentially tracked the same timing noise pattern. The similarity in the timing noise structure is confirmed by the small variation in the RMS values. From Table 4.3 the weighted RMS values ranges from 933 μs to 977 μs, a difference of 45 μs. This is less than 5 % of the mean of the RMS value, indicating that each set of timing residuals bore roughly the same noise level, irrespective of the size of the TOA set.

However, the χ^2_r varied widely depending on the number of TOAs or the number of degrees of freedom (DoF). The DoF is the difference between the number of TOAs and the number of parameters fitted. The relatively low χ^2_r values of the normal mode profiles (2.69 for the set with normal mode template and 2.23 for the abnormal mode template) can be attributed partially to the size of the set of TOAs. It can also be attributed partially to the intrinsic stability of the pulse profile and the consistency in the pulse period when the pulsar is in the normal mode (compare Figure 3.3). This is evident in the better behaved

residuals of the normal mode, having narrow spread about their curves (refer to Figure 4.4 for an example). On the other hand, the relatively large χ^2_r values of the residuals of the abnormal mode (8.79 and 10.54 respectively for the set obtained with the APNT and APAT) indicate a wider spread about the timing model. This can be seen as the result of the smaller number of TOAs used. However, the instability of the pulse profiles, and by extension, the reduced consistency of the TOAs when the pulsar is in the abnormal mode is a more satisfactory explanation (e.g. Chen et al., 2011). This is because the timing solution of the abnormal mode TOAs is almost identical to that of the normal mode TOAs. Nevertheless, the χ^2_r value for all the TOAs (i.e. 2.26 in Table 4.3) is as low as the minimum value recorded, indicating that the normal mode TOAs dominated the final timing solution.

It is well understood that the template plays a crucial role in the accuracy of the TOAs. The template is expected to ideally represent the intrinsic pulses emitted from the pulsar. In practice, the best technique would be used to make template, i.e. a the noiseless replica of the pulse profile, to prevent the correlation of noise that could compromises the accuracy of the TOAs. For a pulsar that changes mode with two distinct pulse profile shapes, the analysis in the sections above suggests that the choice of the template is not the principal cause of offset between the normal and the abnormal mode residuals. The above results show that the differences in the timing solutions of the four sets of TOAs are not highly dependent on the choice of template. Recall that varying the template introduces the greater time offset of $138\,\mu$s, in the residuals of the normal mode profiles than the $82\,\mu$s in that of the abnormal mode profiles. At the same time, the χ^2_r of the former sets are the lowest. Hence, the relatively large χ^2_r values for the residuals of the abnormal mode profiles can be attributed to the small sample size and the reduced stability in both the rotation parameters and pulse profile when the the pulsar is in the abnormal mode.

4.4 Implications of the Two Residual Curves

Given the above conclusions, the deviations of the residuals of the abnormal mode TOAs from that of the normal mode TOAs can be thought of as originating from the pulsar itself. Lyne et al. (2010) demonstrated that variations in pulse shape correlates with the changes in spin-down rate ($\dot{\nu}$) (see also Camilo et al., 2012). Changes in the $\dot{\nu}$ is in turn are thought to arise from the variations in the conditions in the magnetosphere (e.g. Lyne & Graham-Smith, 2005, ; refer to Equation 1.7). Other conditions in the magnetosphere such as the concentration of ionised particles may vary the location of emission source over the surface of the pulsar giving rise to random phase walk of the TOA. These are plausible explanations for the deviations of some timing residuals for PSR B0329+54.

Variations in the moment of inertia can also cause variation in the spin frequency, also known as frequency noise. This is a direct consequence of the spin frequency's dependence on the moment of inertia and the principle of conservation of angular momentum. Sudden and frequent changes in the angular momentum may arise, for example, in the dynamic coupling of the crust and the superfluid stellar interior, as the case may be in the so called "slow glitches" (Shabanova, 1998). However, applying this concept to explain the deviations of the residuals of abnormal mode would mean that the pulsar rapidly changes angular frequency to correspond to the mode switching observed in PSR B0329+54. Given a time interval between mode switching as short as 26 min (Chen et al., 2011), it is not likely that this phenomenon causes frequency noise.

4.5 Mode Switching and Timing Noise

The 3-year periodic structure in the timing residuals (see §2.8), earlier reported by some authors, is the apparent effect of either a persistent condition that is occasionally masked by the long term timing noise or occasionally excited (compare Demiański & Prószyński, 1979; Shabanova, 1995; Starovoit & Rodin, 2017). Here, a modulating component of the residuals with a period of about 185 days is observed, particularly between MJD 56500 and 57500 (see Figure 4.8). A possible link between this periodic modulation in the residuals and the fractional occurrence of the normal mode was analysed.

The smoothed fractional occurrence curves described in §3.3 (Figure 3.6) were used. It was determined by visual inspection that the smoothed curve using 30-day long window with a 10-day stride between the 30-day long window best described the pattern in the fractional occurrence. Since the residual curves for the two modes track each other, that of the normal mode has been used. The plots of the timing residuals and the fractional occurrence are shown in Figure 4.8.

Also, there is a general descending trend in the fractional occurrence with time. Between MJD 55890 and 56459, prior to the start of the periodic modulation event, the number of observations with "pure" mode (observations with fractional occurrence of 1.0 or 0.0) is higher (see Figure 3.6). This gradually decreases during and after the ripple event. This trend in the fractional occurrence implies that the frequency of mode changing increased with time. It also generally implied that the stability of the modes decreased with time.

It can be seen that there is a good correlation between the fractional occurrence and the timing noise during the ripple event between MJD 56459 and 57488. The measured correlation coefficient for this section is 0.6. The correlation is apparently evident in both

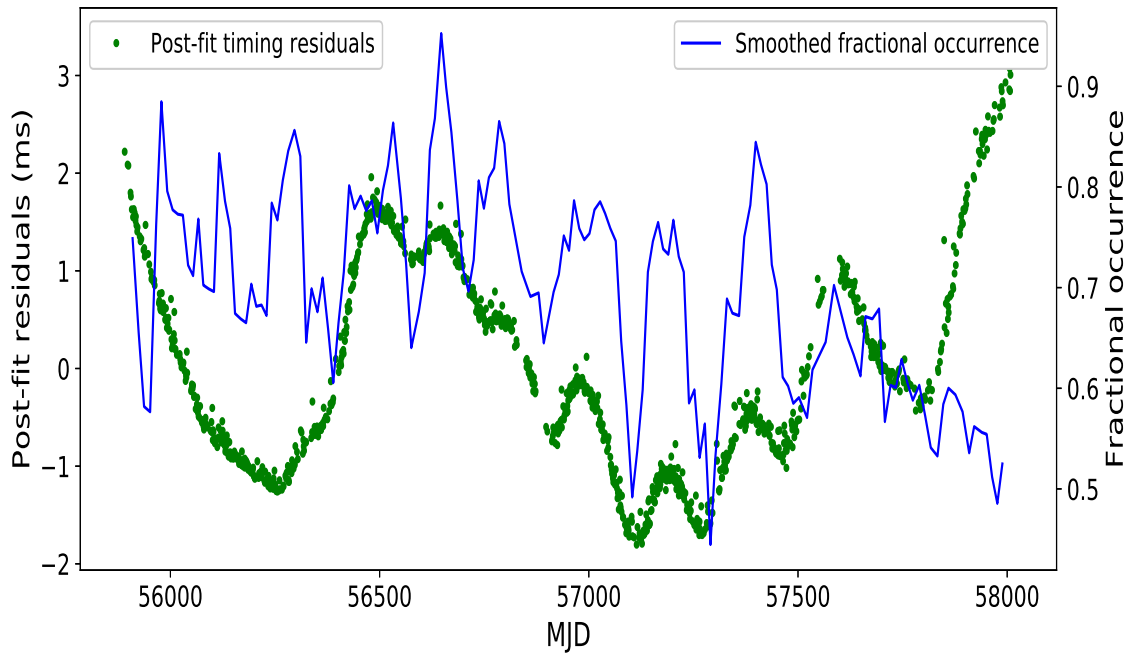

Figure 4.8: The apparent link between the fractional occurrence and the timing noise. There is a good correlation (normalised correlation coefficient of 0.6) between the fractional occurrence and the ripple component of the timing residuals.

the short term ripples and the long term noise components. The fractional occurrence curve also show rapid drops, or dips, that corresponds to the troughs of the ripple. These dips are short lived compared to the peaks. These results imply that during the moments of troughs in the ripples, the pulsar spends less time in the normal mode than it does during the peaks of the ripples. Even though increased stability in the abnormal mode is a possible consequence, the fractional occurrence plot in Figure 3.6 suggest that reduced mode stability, mostly in the normal modes leading to frequent mode switching accounted for the decrease in time spent in the normal mode.

Also, the moving average of the fractional occurrence seems to correlate with the long-term component on the timing residual within the time scale of the ripple event. However, this coherence is absent before and after the ripple event. These results seem

to suggest that the event manifested in the ripple component of the residuals also affected the emission mechanism of the pulsar. The difficulty with this suggestion, however, is that the data have finite time scale, and while the ripple event seem to have ended by MJD 57600, the frequency of the mode switching continued to increase.

4.6 Variation of the Spin-down Rate ($\dot{\nu}$)

The spin-down rate variation is difficult to measure due to the constraint posed by the low order of magnitude of $\dot{\nu}$ (10^{-15}) compared to that of the timing noise ($10^{-9} - 10^{-3}$). Also, long-term observations are required to measure the $\dot{\nu}$ accurately. Alongside the spin irregularity, there is also the finite observation cadence that may compromise the accuracy of fitting the timing model, especially in the case of low observation cadence. Limitations of the observing instruments, ISM and the atmosphere contribute to constraining the TOA precision. These effects increase the overall noise level, making it difficult to measure $\dot{\nu}$ changes over shorter time-scales. Nevertheless, a number of observational evidence suggest that $\dot{\nu}$ varies with time (e.g. Lyne et al., 2010; Camilo et al., 2012; Young et al., 2013).

The observation of intermittent behaviour in PSR B1931+24 and PSR J1841–0500 have shown that $\dot{\nu}$ varies over time in these sources (Kramer et al., 2006; Camilo et al., 2012). For its long time-scale (weeks) stability of "on" and "off" emission states, two discrete values of the spin-down rates were measured, one for each emission state. Some studies have demonstrated correlations between variations in the $\dot{\nu}$ and other pulsar phenomena such as pulse shape (Lyne et al., 2010; Keith et al., 2013; Perera et al., 2015) and nulling (Kramer et al., 2006; Camilo et al., 2012).

Based on the assumption that the timing noise reflects unmodelled effects during

pulsar timing, techniques have been formulated to model the timing noise. The timing noise typically consists of low frequency timing noise and a high frequency uncorrelated noise. Each timing residual value represents a phase of a complete rotation. A continuous model of the timing noise would therefore represent a time-varying function of the spin frequency (ν) and a second derivative of the residuals would represent the time-varying spin-down rate ($\dot{\nu}$) (e.g. Keith et al., 2013). The variation of the spin-down rate of PSR B0329+54 was explored by modelling the timing residuals as a Gaussian process.

4.6.1 Gaussian Process for Measuring Spin-down Rate

Brook et al. (2015) developed a Gaussian process technique to measure the $\dot{\nu}$ variations in 168 pulsars. Their technique was applied to measure the variations of $\dot{\nu}$ of PSR B0329+54. This method assumes that variations in $\dot{\nu}$ account for all the timing noise. It numerically models the residuals and estimate the $\dot{\nu}$ from the model without requiring the second derivative of the timing residuals.

The squared exponential covariance function is used as the kernel because it is infinitely differentiable, allowing a continuous range of functions.

$$k(x_i, x_j) = \sigma_f^2 \exp^{\left(-\frac{d^2}{2\lambda^2}\right)} + \delta_{ij}\sigma_{noise}^2, \tag{4.1}$$

where x_i and x_j are the epochs of the i th and the j th observations respectively, d is the Euclidean distance between the two observations (i.e. $d = |x_i - x_j|$) and λ is a parameter that indicates the significance of the effect of d on the kernel, $k(x_i, x_j)$. λ is also known as the length scale. σ_f^2 is the maximum covariance allowed. σ_{noise}^2 represents the covariance of the white noise component of the residuals. The Kronecker delta, $\delta_{i=j} = 1$ is include to indicate that the covariance of the white noise is evaluated to non-zero only when the

$i = j$ since the white noise are uncorrelated.

Using the Gaussian process, the choice of the parameters of the prior distribution (i.e. the hyper-parameters) is made by maximizing the likelihood. The likelihood is the logarithm of the conditional probability distribution of the expected values given the observation data, expressed as $\log(p(\mathbf{y}|\mathbf{x},\lambda,\sigma_f^2))$, where $\mathbf{y} = \{y_1, y_2, ..., y_i, ...\}$ is the vector of residual values corresponding to the vector of the residual epochs $\mathbf{x} = \{x_1, x_2, ..., x_i, ...\}$.

Let the inferred residual point be (y_*, x_*). Then the covariance matrix of individual covariance between each pair of residuals is defined as $\mathbf{C}_{ij} = k(x_i, x_j)$

$$\mathbf{C}_{ij} = \begin{bmatrix} k(x_1,x_1) & \dots & \dots & \dots & k(x_1,x_n) \\ \vdots & \ddots & \vdots & \dots & \vdots \\ \vdots & \vdots & k(x_i,x_j) & \dots & \vdots \\ \vdots & \vdots & \vdots & \ddots & \vdots \\ k(x_n,x_1) & \dots & \dots & \dots & k(x_n,x_n) \end{bmatrix}, \tag{4.2}$$

for n residuals. Similarly, the matrix that reflects the covariance between the observed residuals to the likely residuals is $\mathbf{C}_* = k(x_*, x_j)$. The inferred value of a residual is given by

$$y_* = \mathbf{C}_* \mathbf{C}_{ij}^{-1} \mathbf{y}. \tag{4.3}$$

The second derivative, together with the optimised parameters, are used to obtain $\dot{\nu}$;

$$\frac{d^2 y_*}{dx^2} = \mathbf{C}_*'' \mathbf{C}_{ij}^{-1} \mathbf{y}, \tag{4.4}$$

where " $'$ " represents derivative with respect to d. The variance of the Gaussian process

is given by

$$var\left(\frac{d^2y_*}{dx^2}\right) = diag(\mathbf{C}_{ij}^{''''}) - \mathbf{C}_*^{''}\mathbf{C}_{ij}^{-1}\mathbf{C}_*^{''}. \quad (4.5)$$

4.6.2 Results of Measuring Spin-down Rate

The technique was implemented using a script written in Fortran. Since the technique requires that every short time-scale of the residuals follow a Gaussian distribution, only the normal mode residuals were used in order to minimise errors in the calculations. Additionally, the curve for the residuals of the normal modes is smoother when we use the the set of normal mode residuals only. Moreover, the residuals for the normal mode are more commonly observed, allowing for accurate calculation of $\dot{\nu}$ at shorter intervals. Finally, since the residual curves of the two modes almost tracked each other, that of the normal mode can be used to represent the underlying timing noise.

The residuals were first modelled with a single covariance function using a length scale constrained between 30 and 1000 days. Figure 4.9 shows the timing residuals fitted with the Gaussian process model. Also shown are the residuals from fitting the Gaussian process model (GP residuals hereafter to distinguish from the timing residuals).

The spin-down rate $\dot{\nu}$ over time calculated from the 2nd derivative of the Gaussian process model is over-plotted on the fractional occurrence curve in Figure 4.10 for comparison. Both plots exhibit harmonic-like modulations and their peaks are broader than the dips. From Figure 4.10 it is clear that a strong correlation exist between the $\dot{\nu}$ and the fractional occurrence during the period of periodic modulation of the timing residuals. Correlation before and after this section of the timing residuals is nearly absent.

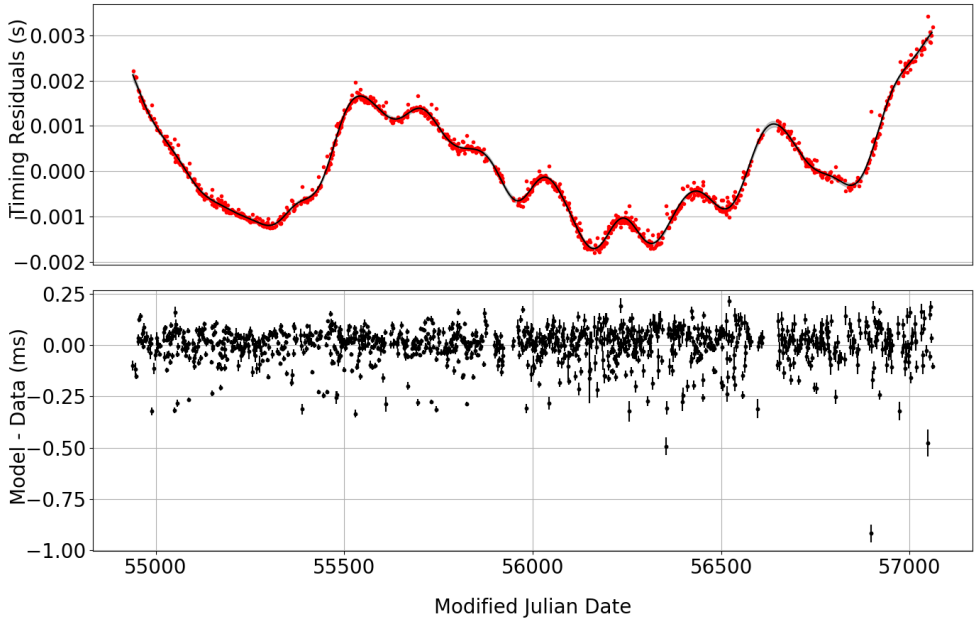

Figure 4.9: The Gaussian process model using a single kernel covariance function with a length scale of 68 days fitted to the timing residuals of PSR B0329+54. Top panel: the timing residuals are represented by the red points and the Gaussian process model is the black trace. A broader trace of $2\,\sigma$ thick represents the range of Gaussian process models that can describe the residuals. Bottom panel: GP residuals at the epochs of observation data. The uncertainties of the GP residuals are those of the timing residuals.

4.7 Possible Mechanism Associated with Mode Changing of PSR B0329+54

The correlation between the fractional occurrence and the spin-down rate suggest a strong link between changes in the magnetosphere and the timing noise consistent with earlier studies (Kramer et al., 2006; Lyne et al., 2010; Camilo et al., 2012). Of particular interest is that the correlation is strongest between MJD 56500 and 57500, the section of the timing residual where there is cyclic modulation structure. Outside this section, correlation is less obvious. It is notable that the range of the $\dot{\nu}$ variability is significantly wider within

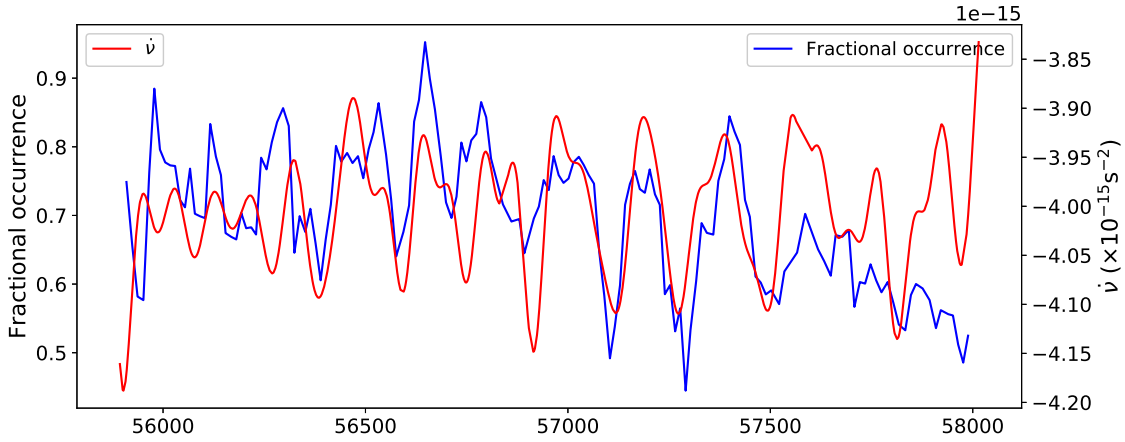

Figure 4.10: The variation of $\dot{\nu}$ (red curve) over plotted on the fractional occurrence curve (blue curve). The error bars are too small to show. The plot shows good correlation between $\dot{\nu}$ and the fractional occurrence between MJD 56500 and 57500.

the same section of the observations. This suggests that the amount of the spin-down may depend on multiple factors and that the condition that excites the periodic modulation also affects $\dot{\nu}$.

A number of mechanisms have been proposed as the possible cause of the nearly harmonic variations in the timing noise. The dependence of the timing noise on the braking torque implies that such mechanism be linked with the distribution of mass of the star. If "slow glitches", i.e. slow rather than sudden increases in spin frequency, are shown to occur periodically and in similar manner, it could be a plausible explanation. This has been suggested to explain the clearly visible cyclic-like structure in the timing noise of PSR B0919+06 (Shabanova, 2010). Vortex lattice oscillation is another possible explanation for the harmonic variation in the timing noise (Ruderman, 1970; Lyne et al., 1988). Some authors have supported the existence of such periodic waves arising from the displacement of the regular lattice structure in the neutron superfluid and used that to explain the modulated periods of 256 and 511 days in the residuals of PSR 1828-11 (Noronha & Sedrakian, 2008; Haskell, 2011). However, it is not clear how these mechanisms are

linked to the mode switching, believed to originate from changes in the magnetosphere.

In addition to causing variation in the angle of inclination between the spin and magnetic axes, models of precession have also been advanced to demonstrate that it can cause such expected mode switching (Jones, 2012). Precession is expected if the neutron star is deformed and the spin axis is not perfectly aligned with the angular momentum vector. The effect is that the star wobbles about its angular momentum vector inclined to the spin axis by a constant angle and completes each precession cycle with the same time period. This effect is expected to reflect in the timing residuals as smooth periodic variations. However, to maintain minimum rotational energy, any process that dissipates energy in the pulsar would contribute to damping precession. Hence long-term precession ($>$ 1 year) observed in a handful of pulsars presents a challenge to the understanding of the internal structure of the neutron stars. Two possible options are that the process that excite the precession persists to sustain the precession or alternatively, recurs with time period shorter than the time it takes to damp the precession.

Jones (2012) argued in support of the possibility of free precession in pulsars with cyclic structures in their residuals. He assumed a biaxial precessing star body. Then the magnetic dipole radiation varies according to both the precession and the spin-down torque. The electric field driving the ionised particles varies accordingly. If the electric field is close to a threshold of two magnetospheric states, then abrupt switches between the two states is possible at various phases of the precession. This argument is consistent with earlier studies by Akgün et al. (2006) in which he used the precession of triaxial model to explain how quasi-periodic structure in the timing residuals of PSR B1828-11 can be generated. The periodic modulation in the timing residual of PSR B0329+54 and its correlation with the fractional occurrence and the $\dot{\nu}$ variations indicates that further comparison with the precession hypothesis is warranted.

Chapter 5

Summary and Conclusions

It is well known that pulsars show spin irregularities that reflect in their timing residuals as timing noise. There have been a number of hypotheses that seek to explain some of the patterns in this timing noise. Some of these hypotheses include: random walk of the spin phase attributed to swapping of the emission source between two or more regions on the surface of the pulsar, or of the spin parameters due to instability of the pulsar's interior superfluid (e.g. Cordes & Downs, 1985); free precession of the star due to asymmetric shape (e.g. Stairs et al., 2000); multiple small glitches (e.g. Janssen & Stappers, 2006; Shabanova, 2010); magnetospheric changes dominated by the magnetic field (e.g. Cheng, 1987); and the effect of the interstellar medium (e.g. Scherer et al., 1997). While each theory applies well to isolated scenarios, multiple mechanisms or conditions may be involved.

There is evidence to suggest that the mechanisms responsible for timing noise also affects other pulsar phenomena. For example, the link between the nulling behaviour of intermittent pulsars, PSR B1931+24 and PSR J1841–0500, with two spin-down rate values (Kramer et al., 2006; Camilo et al., 2012) and the correlation between the variations

in the pulse shapes of some pulsars and their spin-down rate variations (Lyne et al., 2010; Keith et al., 2013; Perera et al., 2015) show that many pulsar phenomena such as timing noise, variations in the pulse shape and/or intensity are manifestations of the same mechanism or conditions.

Even though the mechanism driving these variabilities is not clearly understood, it is believed to originate from variations in the conditions in the magnetosphere. In the plasma-filled configuration of the magnetosphere, radiation is generated by the acceleration of plasma and the cascaded electron-positron pair production. In the vacuum condition of the magnetosphere only the rotating magnetic dipole radiation would be available. Hence the emission mechanism likely varies with magnetospheric changes between these conditions (see Kalapotharakos et al., 2012; Li et al., 2012b).

Another possible explanation is free precession that may cause a smooth periodic variation in the spin-down torque as in the magnetic dipole radiation. Jones (2012) proposed that if the available energy for accelerating plasma for radio emission is close to a threshold, then it may vary about the critical value at some phase of the precession. In such situation the magnetosphere is unstable and switches from one state to the other abruptly.

This study sought to investigate the link between the mode changing and the timing noise of PSR B0329+54. Mode changing/switches in PSR B0329+54 is particularly obvious in the corresponding changes in the intensities of the outer components of the pulse profile. Machine learning algorithms were used to classify observation data into mode classes according to their integrated pulse profiles. The mode of each observation is quantified by the proportion of the normal mode in the observations. This allowed a comparison between the spin parameters and the mode changing. The results are summarised below.

5.1 Summary of the Results

The classification accuracy of the six different machine learning algorithms that were exploited were between 85 and 98 %. We find that features of the classified profiles were consistent with the criteria used to train the algorithms. These show that machine learning is a robust technique for classifying and identifying the profile mode of PSR B0329+54. Also, the fractional occurrence curve shows dips of shorter time-scale but broader peaks indicating that the time-scale of mode changing itself is changing between two states. In addition, the moving average of the fractional occurrence gradually decreases towards 0.5 during the time span of the data set. These show that the mode changing time-scale is changing over time.

It was initially assumed that the offsets between the normal mode and the abnormal mode residuals were as a result of using a template that does not match the pulse profiles of both modes at the same time. To test this, a template of the normal mode shape and another template of the abnormal mode shape were separately matched with the observation profiles to obtain four sets of TOAs. After timing each set separately, it was found that there was an average offset of 138 μs between the two sets of the normal mode residuals and 82 μs between the two sets of the abnormal mode residuals. However, the average time offset between normal mode residuals and abnormal mode residuals were about 4 times greater. Hence the initial assumption cannot be sustained. Rather, the offset of the residuals of the abnormal mode from that of the normal mode may actually be associated with the mode changing of the pulsar. This may imply a random changes of the emission location over the polar cap, introducing a rotation phase difference when the pulsar switches mode.

There is a strong correlation between the fractional occurrence and the periodic modulation of the timing residuals, with a correlation coefficient of about 0.6. Also, between MJD 56500 and 57500, the correlation between the fractional occurrence and the spin-down variations is strong. This agrees with earlier studies that propose that mode changing and nulling reflect magnetospheric state and are consequently linked with the spin-down rate of the pulsar. It further suggest that this association is primarily excited by a cyclic-like mechanism. The nature of this physical mechanism is, however, not clear.

5.2 Conclusions

While pulsar timing noise can be an important source of information about the neutron star interior structure, it limits the use of the pulsar as a precise clock. We can work around this limitation if a model for the timing noise can be found, so that the timing noise can be removed. The apparent link between the spin-down rate variation and the pulse features can be used to probe the origin of the timing irregularities.

In this work we have demonstrated that the time offset between the residuals of the normal and the abnormal modes can be understood to be another manifestation of the mode changing in PSR B0329+54. This would imply that changes in the magnetospheric states are accompanied by changes in the emission location. We have also shown that mode changing correlates with spin-down variation. This means that PSR B0329+54 is a new member of the class of pulsars which show short time-scale mode changes (minutes), as with pulsars like PSR B1828-11 and PSR 1822-09, but that the rate of changing between these modes changes with time and corresponds to changes in the spin-down rate. Having more members in this class will help us find a driving mechanism that links these very different time-scales. This is consistent with earlier studies that suggest that

pulse shape/intensity variation with mode changing is possibly a reflection of changes in the flow of plasma from the pulsar magnetosphere and can consequently be linked to the spin-down variation. However, in this study, we only find this link clearly during the section of the residuals with periodic variations suggesting that the association is excited by an unknown periodic-like mechanism.

Bibliography

Abdo A. A., et al., 2009, The Astrophysical journal letters, 695, L72

Akgün T., Link B., Wasserman I., 2006, Monthly Notices of the Royal Astronomical Society, 365, 653

Aliu E., et al., 2008, Science, 322, 1221

Alpar M., Cheng A., Ruderman M., Shaham J., 1982, Nature, 300, 728

Arons J., Scharlemann E. T., 1979, The Astrophysical Journal, 231, 854

Arzoumanian Z., Nice D., Taylor J., Thorsett S., 1994, The Astrophysical Journal, 422, 671

Baade W., Zwicky F., 1934, Proceedings of the National Academy of Sciences, 20, 254

Backer D., 1970, Nature, 228, 42

Bartel N., Morris D., Sieber W., Hankins T., 1982, The Astrophysical Journal, 258, 776

Beskin V. S., 2009, in , MHD Flows in Compact Astrophysical Objects. Springer, pp 89–175

Beskin V., Gurevich A., Istomin Y. N., 1988, Astrophysics and space science, 146, 205

Bhattacharya D., van den Heuvel E. P. J., 1991, Physics Reports, 203, 1

Biggs J. D., 1992, The Astrophysical Journal, 394, 574

Bignami G., Caraveo P., De Luca A., Mereghetti S., 2003, Nature, 423, 725

Bisnovatyi-Kogan G., Komberg B., 1974, Soviet Astronomy, 18, 217

Boynton P., Groth III E., Partridge R., Wilkinson D. T., 1969, The Astrophysical Journal, 157, L197

Brisken W. F., Benson J. M., Goss W. M., Thorsett S., 2002, The Astrophysical Journal, 571, 906

Brook P., Karastergiou A., Johnston S., Kerr M., Shannon R., Roberts S., 2015, Monthly Notices of the Royal Astronomical Society, 456, 1374

Camilo F., Ransom S., Chatterjee S., Johnston S., Demorest P., 2012, The Astrophysical Journal, 746, 63

Chatterjee P., Hernquist L., Narayan R., 2000, The Astrophysical Journal, 534, 373

Chen J. L., Wang H. G., Wang N., Lyne A., Liu Z. Y., Jessner A., Yuan J. P., Kramer M., 2011, ApJ, 741, 48

Cheng K., 1987, The Astrophysical Journal, 321, 799

Cheng K., Ho C., Ruderman M., 1986, The Astrophysical Journal, 300, 500

Chennamangalam J., Lorimer D., 2014, Monthly Notices of the Royal Astronomical Society: Letters, 440, L86

Cole T. W., Pilkington J. D. H., 1968, Nature, 219

Cordes J., Downs G., 1985, The Astrophysical Journal Supplement Series, 59, 343

Cordes J., Helfand D., 1980, The Astrophysical Journal, 239, 640

Cordes J. M., Lazio T. J. W., 1997, The Astrophysical Journal, 475, 557

Cordes J., Shannon R., 2008, The Astrophysical Journal, 682, 1152

Deich W., Cordes J., Hankins T., Rankin J., 1986, The Astrophysical Journal, 300, 540

Demiański M., Prószyński M., 1979, Nature, 282, 383

Demorest P. B., et al., 2012, The Astrophysical Journal, 762, 94

Esamdin A., Lyne A., Graham-Smith F., Kramer M., Manchester R., Wu X., 2005, Monthly Notices of the Royal Astronomical Society, 356, 59

Espinoza C. M., Lyne A. G., Stappers B. W., Kramer M., 2011, Monthly Notices of the Royal Astronomical Society, 414, 1679

Foster R., Fairhead L., Backer D., 1991, The Astrophysical Journal, 378, 687

Gangadhara R., Gupta Y., 2001, The Astrophysical Journal, 555, 31

Gangadhara R., Gupta Y., Lorimer D., 2000, in International Astronomical Union Colloquium. pp 163–164

Gil J., Kijak J., Seiradakis J., 1993, Astronomy and Astrophysics, 272, 268

Gold T., 1968, Nature, 218, 731

Goldreich P., Julian W. H., 1969, The Astrophysical Journal, 157, 869

Grindlay J., Camilo F., Heinke C., Edmonds P., Cohn H., Lugger P., 2002, The Astrophysical Journal, 581, 470

Gunn J. E., Ostriker J. P., 1969, Nature, 221, 454

Haskell B., 2011, Physical Review D, 83, 043006

Haskell B., Melatos A., 2015, International Journal of Modern Physics D, 24, 1530008

Helfand D., Manchester R., Taylor J., 1975, The Astrophysical Journal, 198, 661

Hermsen W., et al., 2013, Science, 339, 436

Hesse K., 1973, Astronomy and Astrophysics, 27, 373

Hewish A., Bell S. J., Pilkington J., Scott P. F., Collins R. A., 1968, Nature, 217, 709

Hirotani K., 2008, The Astrophysical Journal Letters, 688, L25

Hobbs G., et al., 2010a, Classical and Quantum Gravity, 27, 084013

Hobbs G., Lyne A., Kramer M., 2010b, Monthly Notices of the Royal Astronomical Society, 402, 1027

Hotan A. W., Van Straten W., Manchester R., 2004, Publications of the Astronomical Society of Australia, 21, 302

Imshennik V., 1995, Space Science Reviews, 74, 325

Jackson J., 1962, Wiley, New York.

Janssen G. H., Stappers B., 2006, Astronomy & Astrophysics, 457, 611

Jones D., 2012, Monthly Notices of the Royal Astronomical Society, 420, 2325

Kalapotharakos C., Kazanas D., Harding A., Contopoulos I., 2012, The Astrophysical Journal, 749, 2

Karastergiou A., et al., 2001, Astronomy & Astrophysics, 379, 270

Karastergiou A., Johnston S., Kramer M., Bhat N., Gupta Y., 2004, in Symposium-International Astronomical Union. pp 337–338

Keane E. F., Kramer M., Lyne A. G., Stappers B. W., McLaughlin M. A., 2011, Monthly Notices of the Royal Astronomical Society, 415, 3065

Keane E., et al., 2014, arXiv preprint arXiv:1501.00056

Keith M. J., Shannon R. M., Johnston S., 2013, MNRAS, 432, 3080

Kijak J., Gil J., 1997, Monthly Notices of the Royal Astronomical Society, 288, 631

Konacki M., Lewandowski W., Wolszczan A., Doroshenko O., Kramer M., 1999, The Astrophysical Journal Letters, 519, L81

Kramer M., 1994, Astronomy and Astrophysics Supplement Series, 107

Kramer M., Wielebinski R., Jessner A., Gil J., Seiradakis J., 1994, Astronomy and Astrophysics Supplement Series, 107

Kramer M., Jessner A., Doroshenko O., Wielebinski R., 1997, ApJ, 488, 364

Kramer M., Karastergiou A., Gupta Y., Johnston S., Bhat N., Lyne A., 2003, Astronomy & Astrophysics, 407, 655

Kramer M., Lyne A. G., O'Brien J. T., Jordan C. A., Lorimer D. R., 2006, Science, 312, 549

Krawczyk A., Lyne A., Gil J., Joshi B. C., 2003, Monthly Notices of the Royal Astronomical Society, 340, 1087

Kuzmin A., Izvekova V., 1996, in International Astronomical Union Colloquium. pp 217–219

Li J., Spitkovsky A., Tchekhovskoy A., 2012a, The Astrophysical Journal, 746, 60

Li J., Spitkovsky A., Tchekhovskoy A., 2012b, The Astrophysical Journal Letters, 746, L24

Lin J.-R., Zhang S., 2004, The Astrophysical Journal Letters, 615, L133

Lorimer D., 2001, Binary and millisecond pulsars at the new millennium

Lorimer D. R., Kramer M., 2005a, Handbook of pulsar astronomy. Vol. 4, Cambridge University Press

Lorimer D. R., Kramer M., 2005b, Handbook of pulsar astronomy. Vol. 4, Cambridge University Press

Lorimer D., Lyne A., McLaughlin M., Kramer M., Pavlov G., Chang C., 2012, The Astrophysical Journal, 758, 141

Lyne A., 1971, Monthly Notices of the Royal Astronomical Society, 153, 27P

Lyne A., 1999, in Pulsar Timing, General Relativity and the Internal Structure of Neutron Stars. p. 141

Lyne A., Graham-Smith F., 2005, Pulsar astronomy. No. 48, Cambridge University Press

Lyne A. G., Smith F., Graham D., 1971, Monthly Notices of the Royal Astronomical Society, 153, 337

Lyne A., Pritchard R., Smith F. G., 1988, Monthly Notices of the Royal Astronomical Society, 233, 667

Lyne A., Pritchard R., Shemar S., 1995, Journal of Astrophysics and Astronomy, 16, 179

Lyne A., Hobbs G., Kramer M., Stairs I., Stappers B., 2010, Science, 329, 408

Manchester R. N., Hobbs G. B., Teoh A., Hobbs M., 2005, The Astronomical Journal, 129, 1993

Maron O., Kijak J., Kramer M., Wielebinski R., 2000, Astronomy and Astrophysics Supplement Series, 147, 195

Melikidze G., Gil J., 2006, Chinese Journal of Astronomy and Astrophysics, 6, 81

Melrose D., 1995, Journal of Astrophysics and Astronomy, 16, 137

Mestel L., 1971, Nature, 233, 149

Michel F. C., Li H., 1999, Physics reports, 318, 227

Noronha J., Sedrakian A., 2008, Physical Review D, 77, 023008

Pacini F., 1967, Nature, 216, 567

Pedregosa F., et al., 2011, Journal of Machine Learning Research, 12, 2825

Perera B. B. P., Stappers B. W., Weltevrede P., Lyne A. G., Bassa C. G., 2015, MNRAS, 446, 1380

Petit G., Tavella P., 1996, Astronomy and Astrophysics, 308, 290

Pons J. A., Walter F. M., Lattimer J. M., Prakash M., Neuhäuser R., An P., 2002, The Astrophysical Journal, 564, 981

Popov M. V., et al., 2016, Monthly Notices of the Royal Astronomical Society, 465, 978

Radhakrishnan V., Manchester R., 1969, Nature, 222, 228

Radhakrishnan V., Cooke D., Komesaroff M., Morris D., 1969, Nature, 221, 443

Rankin J. M., 1990, The Astrophysical Journal, 352, 247

Ritchings R., 1976, Monthly Notices of the Royal Astronomical Society, 176, 249

Romani R. W., 1996, The Astrophysical Journal, 470, 469

Ruderman M., 1969, Nature, 223, 597

Ruderman M., 1970, Nature, 225, 619

Ruderman M., 1974, in Symposium-International Astronomical Union. pp 117–131

Ruderman M. A., Sutherland P. G., 1975, The Astrophysical Journal, 196, 51

Samuel A. L., 1959, IBM Journal of Research and Development, 3, 210

Scherer K., Fichtner H., Anderson J. D., Lau E. L., 1997, Science, 278, 1919

Shabanova T. V., 1995, The Astrophysical Journal, 453, 779

Shabanova T., 1998, Astronomy and Astrophysics, 337, 723

Shabanova T. V., 2010, The Astrophysical Journal, 721, 251

Shang L.-H., et al., 2017, Monthly Notices of the Royal Astronomical Society, 468, 4389

Shemar S., Lyne A., 1996, Monthly Notices of the Royal Astronomical Society, 282, 677

Spitkovsky A., 2004, in Symposium-International Astronomical Union. pp 357–364

Staelin D. H., Reifenstein E. C., 1968, Science, 162, 1481

Stairs I., Lyne A., Shemar S., 2000, Nature, 406, 484

Starovoit E., Rodin A., 2017, Astronomy Reports, 61, 948

Sturrock P., 1971, The Astrophysical Journal, 164, 529

Suleĭmanova S. A., Pugachev V. D., 2002, Astronomy Reports, 46, 34

Takata J., Shibata S., Hirotani K., 2004, Monthly Notices of the Royal Astronomical Society, 354, 1120

Tan C. M., 2014, Using Machine Learning to Identify Differences in the Emission from Radio Pulsars

Tauris T. M., et al., 2014, arXiv preprint arXiv:1501.00005

Taylor J. H., 1992, Philosophical Transactions of the Royal Society of London A: Mathematical, Physical and Engineering Sciences, 341, 117

Taylor J., Manchester R., Huguenin G., 1975, The Astrophysical Journal, 195, 513

Timokhin A., 2010, Monthly Notices of the Royal Astronomical Society: Letters, 408, L41

Tsuruta S., Canuto V., Lodenquai J., Ruderman M., 1972, The Astrophysical Journal, 176, 739

Wang N., Manchester R. N., Pace R., Bailes M., Kaspi V. M., Stappers B., Lyne A. G., 2000, Monthly Notices of the Royal Astronomical Society, 317, 843

Wang N., Manchester R., Johnston S., 2007, Monthly Notices of the Royal Astronomical Society, 377, 1383

Wang H.-G., Chen J.-L., Wen Z.-G., Pi F.-P., 2012, Proceedings of the International Astronomical Union, 8, 549

Wu X., Gao X., Rankin J. M., Xu W., Malofeev V. M., 1998, The Astronomical Journal, 116, 1984

Xu R., Qiao G., 2001, The Astrophysical Journal Letters, 561, L85

Young N., Stappers B., Lyne A., Weltevrede P., Kramer M., Cognard I., 2013, Monthly Notices of the Royal Astronomical Society, 429, 2569

Zhang B., Gil J., Dyks J., 2007, Monthly Notices of the Royal Astronomical Society, 374, 1103

van Straten W., Bailes M., 2011, Publications of the Astronomical Society of Australia, 28, 1